Energy & Buildings 359 (2026) 117245

Contents lists available at ScienceDirect

Energy & Buildings

journal homepage: www.elsevier.com/locate/enb

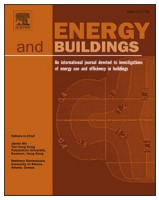

Effects of cool coatings on urban microclimate and outdoor thermal comfort: A CFD–CitySim pro coupled simulation study

Da-Som Mun [a], Jérôme Henri Kämpf [b], Jae-Jin Kim [a,c,*]

[a] Division of Earth and Environmental System Sciences, Pukyong National University, Busan, the Republic of Korea
[b] Energy Informatics Group, Idiap Research Institute, Rue Marconi 19, 1920 Martigny, Switzerland
[c] Research & Management Center for Particulate Matter in the Southeast Region of Korea, Ulsan National Institute of Science and Technology, Ulsan, the Republic of Korea

ARTICLE INFO

Keywords:
CitySim Pro
CFD model
Cool coating materials
Pedestrian thermal comfort
Urban heat environment

ABSTRACT

This study examines how cool coatings, which modify the radiative properties of building and ground surfaces, affect urban microclimate and pedestrian thermal comfort in a district with heterogeneous building heights. A computational fluid dynamics (CFD) model coupled with CitySim Pro explicitly resolved shortwave and long-wave radiative exchanges. The framework was validated against field measurements, demonstrating high accuracy for surface/air temperatures and wind speed/direction in the control experiment (CNTL) using in-situ material properties. Sensitivity experiments revealed that high-rise facade coatings (BiGc, BiGj) reduced the coated facade surface temperature by 4.70–5.56℃, but increased temperatures on nearby low-rise facades and roofs by up to 6.03℃ and 4.06℃, respectively. In the combined case (BiGj), adding high-reflectance pavement mitigated the facade-induced ground warming observed in BiGc by ~ 2℃. Ground-only coatings (BcGj) lowered pavement temperature by 1.71–2.24℃ while producing only minor thermal changes on surrounding buildings. Regarding air temperature, ground-only coatings produced marginal nighttime cooling and ~ 0.5℃ daytime cooling, primarily over open spaces. Facade-involved scenarios achieved up to 2℃ daytime cooling near deep canyons but caused localized nocturnal warming of 0.3–2.0℃ in medium and shallow canyons. Universal Thermal Climate Index (UTCI) analysis at the Gwanghwamun Square showed ground-only coatings increased daytime UTCI by < 1℃ on average, whereas facade-involved treatments raised UTCI by up to 4.13℃ due to intensified mean radiant temperature. Overall, ground-centric coatings minimize comfort penalties, while facade treatments require strict radiative control. Prioritizing shaded ground applications in high-activity areas offers a practical balance between urban cooling and pedestrian well-being.

1. Introduction

The development and application of novel materials have diversified urban surface covers and directly influence the radiative properties of building facades and ground surfaces–particularly surface temperature [1–4]. As urbanization intensifies, the expansion of impervious surfaces progressively degrades the urban thermal environment, prompting the implementation of mitigation strategies such as vegetation and water bodies [5–9]. However, installation and life-cycle maintenance costs, alongside spatial constraints in high-density districts, often limit the city-wide development of these nature-based solutions [10].

In light of these limitations, cool surface materials—most notably high-albedo finishes and cool coatings—have emerged as cost-effective heat-mitigation options [11–15]. By increasing short-wave albedo, these materials reduce radiative energy absorption and lower surface temperatures. In particular, cool-coating techniques are highly

Abbreviations: ACH, Air Changes per Hour; ASOS, Automated Synoptic Observation System; BES, Building Energy Simulation; CFD, Computational Fluid Dynamics; CIM, Canopy Interface Model; CNTL, Control experiment; DHD, dense high-rise district; DLD, dense low-rise district; GIS, Geographic Information System; H, building height; HVAC, Heating, Ventilation, and Air Conditioning; IOA, Index of Agreement; JRC, Joint Research Centre; KMA, Korea Meteorological Administration; LST, Local Standard Time; OSD, open space district; PVGIS, Photovoltaic Geographical Information System; RMSE, Root Mean Square Error; RNG k-ε, Renormalization Group k-epsilon; SLD, sheltered low-rise district; UTCI, Universal Thermal Climate Index; UWG, Urban Weather Generator.

* Corresponding author at: Division of Earth and Environmental System Sciences, Pukyong National University, 45, Yongso-ro, Nam-Gu, Busan 48513, the Republic of Korea.
E-mail address: jjkim@pknu.ac.kr (J. Kim).

https://doi.org/10.1016/j.enbuild.2026.117245
Received 30 November 2025; Received in revised form 31 January 2026; Accepted 26 February 2026
Available online 3 March 2026

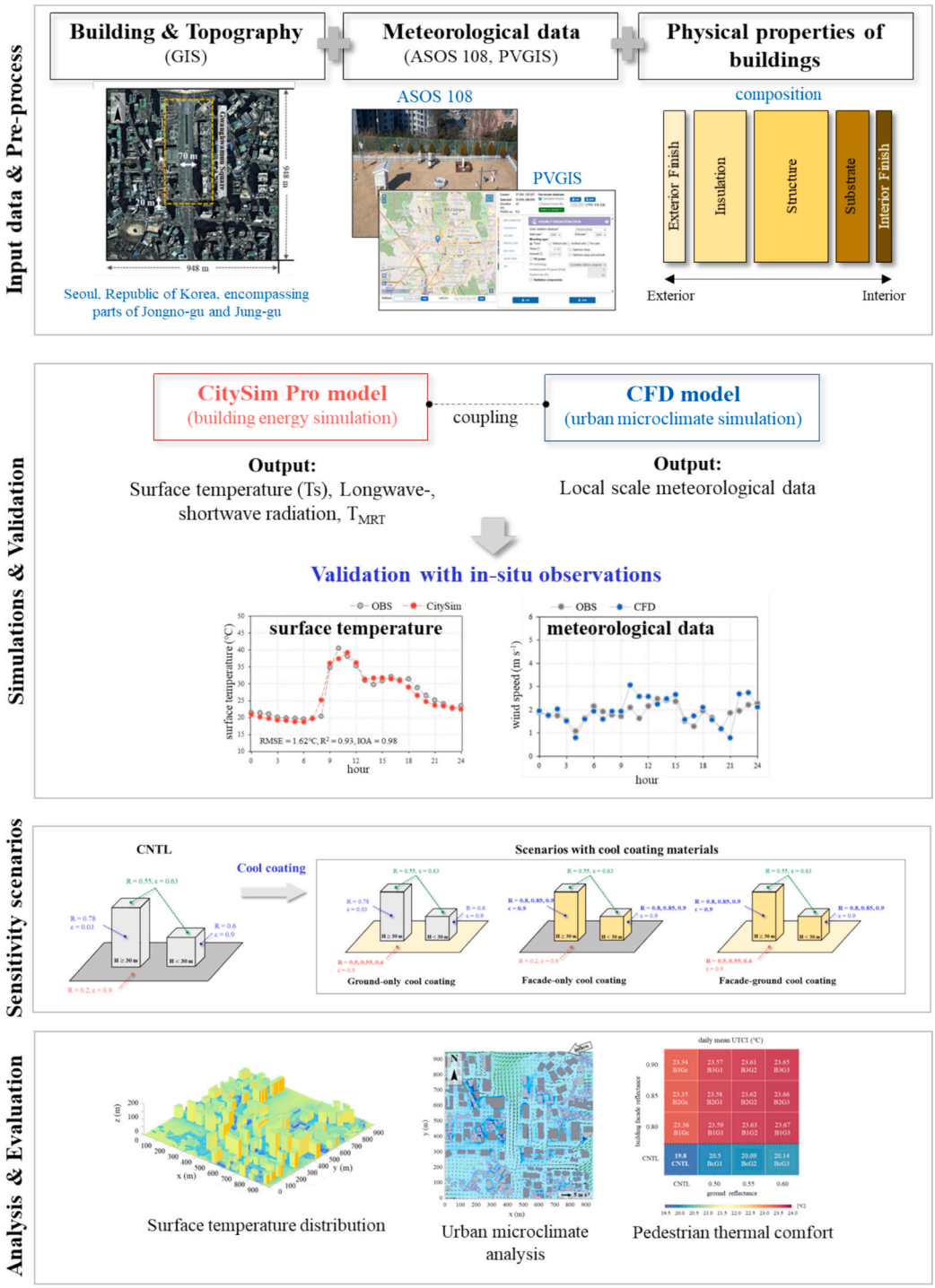

Fig. 1. Research flowchart illustrating the integrated simulation framework, scenario design, and evaluation process for urban microclimate and thermal comfort analysis.

economical, as they can be applied directly to facades or ground surfaces without structural alteration. Furthermore, they have demonstrated significant summer benefits for indoor thermal conditions and cooling energy efficiency [16]. While vegetation-based strategies provide superior pedestrian comfort through simultaneous shading and evapotranspiration, their application is often constrained by urban density and spatial requirements [17,18]. In high-density environments where large-scale greenery is impractical, cool coatings serve as a complementary or alternative solution for cost-effective heat mitigation. However, their implementation must be carefully managed to avoid potential radiative penalties to pedestrians, particularly in open urban settings where reflected radiation can significantly elevate the mean radiant temperature. Furthermore, regarding seasonal trade-offs, while winter heating penalties warrant consideration, previous studies report that wintertime surface-temperature contrasts between cool surfaces and conventional ones are often modest, suggesting limited adverse impacts during the heating season [16,19,20].

Recent in-situ campaigns and numerical studies have analyzed the effects of cool materials on urban thermal environments and energy efficiency [21–26]. Shen et al. [27] showed from summer-winter

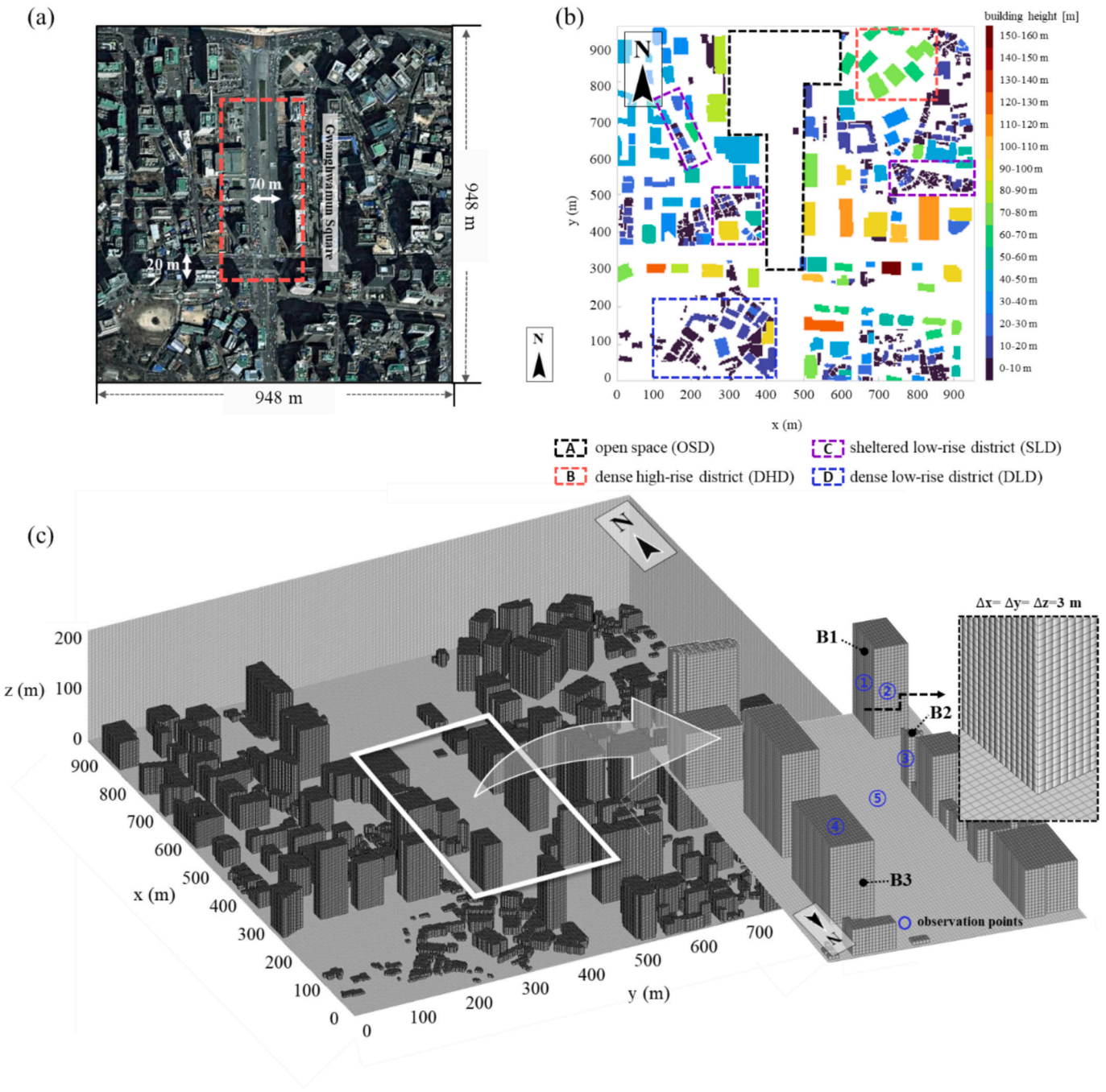

Fig. 2. Overview of the target area and simulation setup: (a) Satellite image of the target area in Seoul (the pink dashed line indicates Gwanghwamun Square); (b) building configuration for the CitySim Pro and CFD simulations, where the color scale represents building heights (m), and annotations A, B, C, and D indicate the open space (OSD), dense high-rise (DHD), sheltered low-rise (SLD), and dense low-rise districts (DLD), respectively.; and (c) three-dimensional CFD mesh layout, where numbered markers ①-⑤ indicate surface temperature measurement points used for validation. (For interpretation of the references to colour in this figure legend, the reader is referred to the web version of this article.)

experiments on a single building with solar-reflective coatings that cooling demand decreased in summer, whereas heating demand increased in winter. Early radiative-only studies investigated sensitivities of surface/air temperature, mean radiant temperature (T_{mrt}), and Universal Thermal Climate Index (UTCI) to albedo and aspect ratio in idealized street canyons [28,29], while more recent computational fluid dynamics (CFD) models coupled with radiation modules quantified the joint roles of radiation and airflow in realistic urban settings [30–36]. Collectively, these studies indicate that cool materials reduce summer surface temperatures, improve outdoor thermal environments, and can lower energy demand, but a recurring caveat is local comfort degradation at pedestrian height due to enhanced reflections [37–39].

Urban surface materials are design levers that regulate solar gains and thermal fluxes in a warming climate where heatwaves and tropical nights occur more frequently [40]. Recently, various numerical simulation frameworks have been successfully utilized for urban energy and microclimate analysis, each offering distinct advantages depending on the research scale and objectives. URBANopt, an EnergyPlus-based urban energy simulation tool, and Ladybug Tools, integrated with Grasshopper, are widely recognized for their efficiency in district-scale energy modeling [41,42]. Additionally, the Urban Weather Generator (UWG) provides valuable insights into the urban canopy layer by

Table 1
Composite material composition of wall, roof, floor, and ground.

Wall	Material	Conductivity (W/m•K)	Cp (J/kg•K)	Density (kg/m^3)	Thickness (m)	Remarks
	aluminum panel	160	880	2800	0.003	building height ≥ 30 *m*
	ceramic tile	1	1000	1900	0.01	building height < 30 *m*
	expanded polystyrene (EPS): 15–40 kg/m^3	0.048	1450.8	40	0.015 ~ 0.190	thickness varies depending on a building type (U-value).
	reinforced concrete (with 2% steel)	2.5	1000.8	2400	0.2	–
	gypsum plasterboard CEN	0.25	1051.2	900	0.025	–
	acryl paint	0.2	1400	1050	0.005	–
Roof	concrete tile	1.5	1000	2100	0.02	
	PE polyethylene CEN	0.05	2300.4	70	0.005	
	cement mortar	1.4	1100	2200	0.1	
	reinforced concrete (with 2% steel)	2.5	1000.8	2400	0.3	
	expanded polystyrene (EPS): 15–40 kg/m^3	0.048	1450.8	40	0.029 ~ 0.3	thickness varies depending on a building type (U-value).
	gypsum plasterboard CEN	0.25	1051.2	900	0.0125	
Floor	expanded polystyrene (EPS): 15–40 kg/m^3	0.048	1450.8	40	0.005 ~ 0.21	thickness varies depending on a building type (U-value).
	reinforced concrete (with 2% steel)	2.5	1000.8	2400	1	
	cement mortar	1.4	1100	2200	0.1	
	ceramic tile	1.3	838.8	2300	0.012	
Ground	cast asphalt	0.7	1100	2150	0.025	
	soil, sand and gravel	2	1051.2	2000	0.02	
	gravel	2	1051.2	2000	0.1	
	soil, clay or slime	1.5	2098.8	1500	0.155	

Table 2
Composition of ceramic coating and cool paint materials.

Material	Conductivity (W/m•K)	Cp (J/kg•K)	Density (kg/m^3)	Thickness (m)	Remarks
Ceramic coating	1.2	796	2000	0.002	–
Cool paint	0.09	800	1053	0.0005 (wall) 0.002 (ground)	–

effectively linking mesoscale climate data in rural areas with micro-scale energy demands [43]. While these tools are highly effective for their intended scales, high-resolution analysis of complex radiative exchanges and localized airflow patterns in high-density urban canyons often requires CFD approaches that explicitly resolve geometry-induced flow and heat transfer. Accordingly, recent studies have increasingly employed OpenFOAM-based CFD models with integrated radiation modules [44]. Building on these advancements, this study enhances simulation fidelity by coupling a CFD model with CitySim Pro model. In this coupled framework, CitySim Pro computes time-varying surface temperatures by explicitly accounting for the thermal inertia and multi-layered thermophysical properties of building assemblies, while the CFD model resolves micro-scale airflow and the resulting convective heat transfer at pedestrian height. Importantly, this approach is not intended to replace existing urban energy or microclimate frameworks; rather, it provides a specialized methodology for real-world, high-density districts where detailed surface–air interactions, radiative heterogeneity (e.g., facade–ground contrasts), and localized airflows must be represented simultaneously. More broadly, the proposed workflow is a form of building energy simulation (BES)–CFD coupling. Coupling building energy simulation (BES) with CFD models improves realism by providing time-varying surface temperatures and energy demand from material/assembly properties and indoor-outdoor exchanges [45,46], and by resolving micro-scale airflow and heat transfer linked to geometry and openings [47–50]. Such coupling can change outdoor comfort metrics by up to ~ 40% [51,52] and enhances simulation fidelity for street-canyon heat fluxes and pedestrian comfort [53–56]. Nevertheless, many previous studies assume uniform albedo in simplified forms or treat isolated buildings, whereas city-scale analyses often lack spatial

Table 3
Radiative properties in CNTL and the sensitivity experiments.

	CNTL	BiGj														
		B1Gc	B2Gc	B3Gc	BcG1	BcG2	BcG3	B1G1	B1G2	B1G3	B2G1	B2G2	B2G3	B3G1	B3G2	B3G3
	R/ε															
Facade (building height > 30 m)	0.78/0.03	0.8/0.9	0.85/0.9	0.9/0.9	–	–	–	0.8/0.9	0.8/0.9	0.8/0.9	0.85/0.9	0.85/0.9	0.85/0.9	0.9/0.9	0.9/0.9	0.9/0.9
Facade (building height ≤ 30 m)	0.6/0.9	0.8/0.9	0.85/0.9	0.9/0.9	–	–	–	0.8/0.9	0.8/0.9	0.8/0.9	0.85/0.9	0.85/0.9	0.85/0.9	0.9/0.9	0.9/0.9	0.9/0.9
Ground	0.2/0.9	–	–	–	0.5/0.9	0.55/0.9	0.6/0.9	0.5/0.9	0.55/0.9	0.6/0.9	0.5/0.9	0.55/0.9	0.6/0.9	0.5/0.9	0.55/0.9	0.6/0.9
Roof	0.55/0.63	–	–	–	–	–	–	–	–	–	–	–	–	–	–	–

* Here, *R* and ε denote reflectance and longwave emissivity, respectively. Uppercase letters, B and G, indicate experiments involving changes in the *R* and ε for building facades and ground surfaces, respectively. Lowercase letter, c denotes the same R and ε used in the CNTL. i = 1, 2, 3 indicates experiments where the *R* of building facade materials is 0.8, 0.85, and 0.9, respectively, while j = 1, 2, 3 indicates experiments where the *R* of ground surface materials is 0.5, 0.55, and 0.6, respectively.

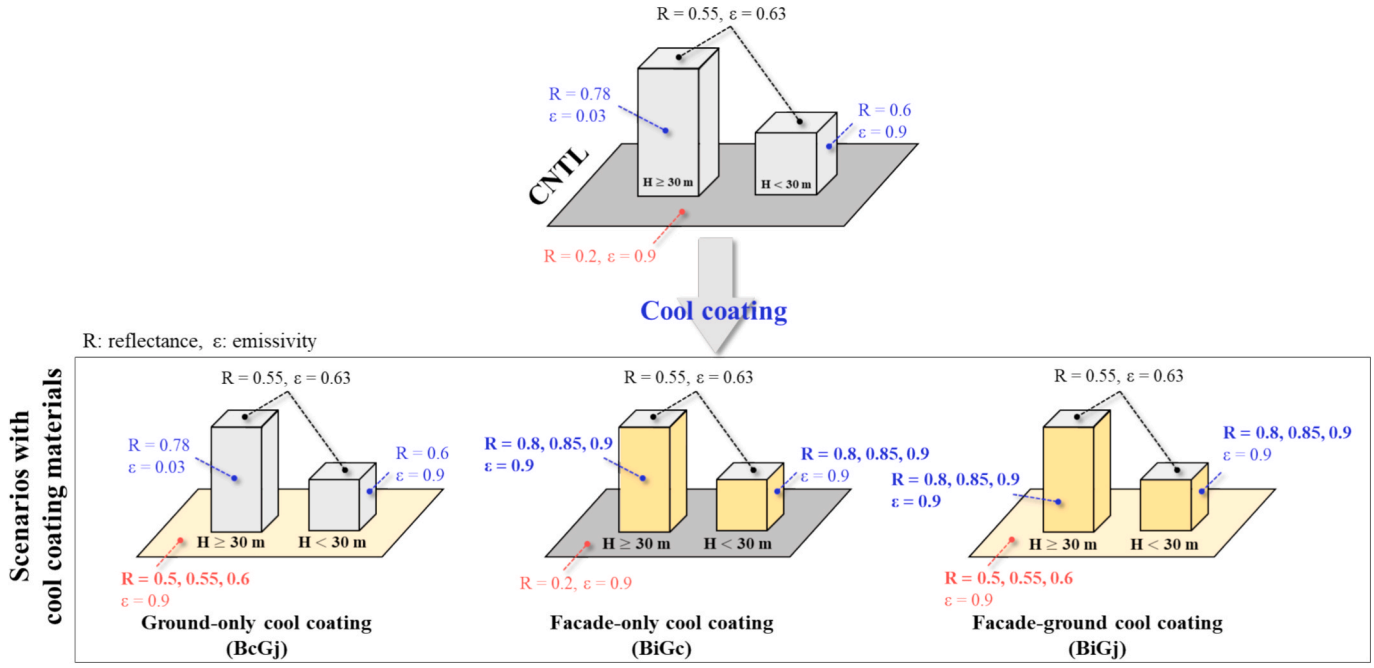

Fig. 3. Conceptual illustration of the control experiment (CNTL) and scenarios with cool coating materials. The symbols R and ε represent solar reflectance and long-wave emissivity, respectively.

resolution to capture heterogeneity in densely built-up areas [37,57]. Few have jointly tested building facade- and ground-surface modifications while assessing the coupled surface–air temperature field and pedestrian height thermal comfort in complex, real-world settings [34,37,58].

To address these gaps, this study coupled the CitySim Pro model with a CFD model to quantify how cool coatings applied to both facades and ground surfaces reshape the radiative energy balance and near-surface microclimate in a dense urban district. Surface temperatures predicted by CitySim Pro model drive the boundary conditions of the CFD model, enabling high-resolution, physically consistent simulations of surface-air interactions. Microclimate impacts—including surface and air temperatures, wind fields, and pedestrian height thermal comfort—under building facade-only, ground-only, and combined-application scenarios are evaluated.

2. Methodology

The overall research framework, illustrating the integrated simulation process and experimental design, is presented in Fig. 1. Section 2.1 describes the CitySim Pro model, focusing on the dynamic surface energy balance and the calculation of time-varying surface temperatures for complex urban geometries. Section 2.2 introduces the numerical framework of the computational fluid dynamics (CFD) model and its specific configuration for urban microclimate simulation. The comprehensive simulation setup—encompassing the computational domain, grid generation, and the prescription of initial and boundary conditions—is detailed in Section 2.3. Finally, Section 2.4 presents the Universal Thermal Climate Index (UTCI) as the primary metric for evaluating outdoor thermal comfort at the pedestrian height.

2.1. CitySim pro model

Accurate prediction of building facade and ground surface temperatures requires a numerical model that quantitatively represents the thermal properties of individual surfaces. Therefore, this study employed the CitySim Pro model, an urban energy modeling tool that resolves surface-temperature evolution in multi-layer assemblies by explicitly modeling radiative exchange and urban surface characteristics across scales, from single buildings to city-wide level [59,60]. The CitySim Pro model estimates surface temperatures and predicts building energy performance by accounting for short-wave and long-wave radiation balance, as well as short-wave reflectance (albedo). This index is a critical determinant of solar accessibility and radiative exchange within urban canyons. The simulation of building thermal behavior is based on a simplified dynamic thermal balance using a Resistor-Capacitor (RC) network model. In this framework, thermal inertia and heat transfer paths within building elements are represented by thermal capacitance and resistance, respectively [61]. The hourly thermal load is determined by integrating external radiative fluxes—including multi-reflections and shading within urban canyons—with conductive heat transfer based on physical parameters (thermal conductivity, thickness, and insulation), and internal heat gains. Passive strategies, such as natural ventilation, are incorporated via a prescribed ventilation rate (Air Changes per Hour, ACH). For this study, an ACH of 0.1 h^{-1} was applied, assuming a standard office schedule with indoor setpoint temperatures maintained between 20℃ and 26℃. Given that the target period is characterized by dominant summer cooling conditions, mechanical HVAC (heating, ventilation, and air conditioning) operation was the primary driver of energy demand. Following established methodologies [54–56,62], the surface temperatures predicted by the CitySim Pro model were utilized as boundary conditions in the CFD simulations. This integrated approach ensures that the urban surface thermal characteristics are accurately incorporated to analyze the high-resolution, near-surface thermal environments.

2.2. Computational fluid dynamics (CFD) model

This study employed the same CFD model as that in Mun et al. [63], which is based on the Reynolds-averaged Navier–Stokes equations. The model assumes unsteady, non-hydrostatic, and non-rotational airflow, and adopts the Boussinesq approximation to represent buoyancy effects in urban environments, turbulent flows are parameterized using the RNG k-ε turbulence closure scheme, and the governing equations are numerically solved using the finite volume method combined with the semi-implicit method for pressure-linked equations algorithm on a

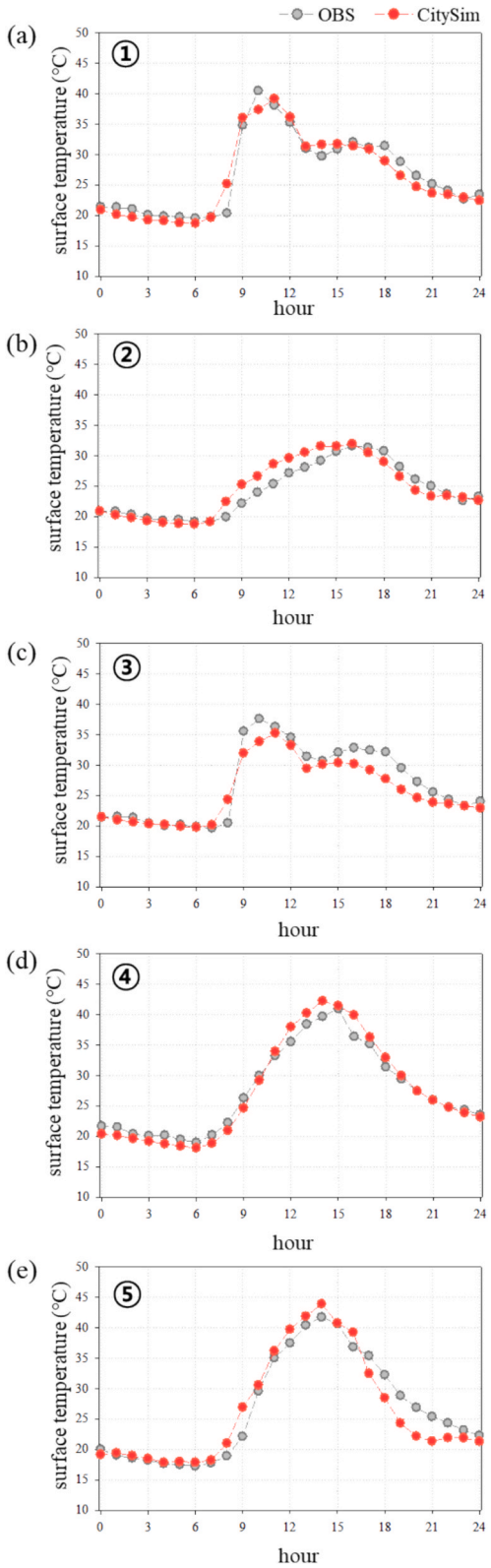

Fig. 4. Comparison of surface temperatures measured by Kim et al. [107] (grey symbols) and simulated by the CitySim Pro model (orange symbol) at locations (a) ①, (b) ②, (c) ③, (d) ④, and (e) ⑤ as indicated in Fig. 2c, from 00:00 to 24:00 LST (local standard time) on 7 September 2015. (For interpretation of the references to colour in this figure legend, the reader is referred to the web version of this article.)

Table 4
Summary of statistical indicators, including Root Mean Square Error (RMSE), Coefficient of Determination (R^2), and Index of Agreement (IOA), for the validation of surface temperatures simulated by the CitySim Pro model.

	building facade (①)	building facade (②)	building facade (③)	rooftop (④)	ground (⑤)
RMSE	1.62℃	1.64℃	2.14℃	1.41℃	2.37℃
R^2	0.93	0.87	0.94	1.00	0.92
IOA	0.98	0.96	0.96	0.99	0.98

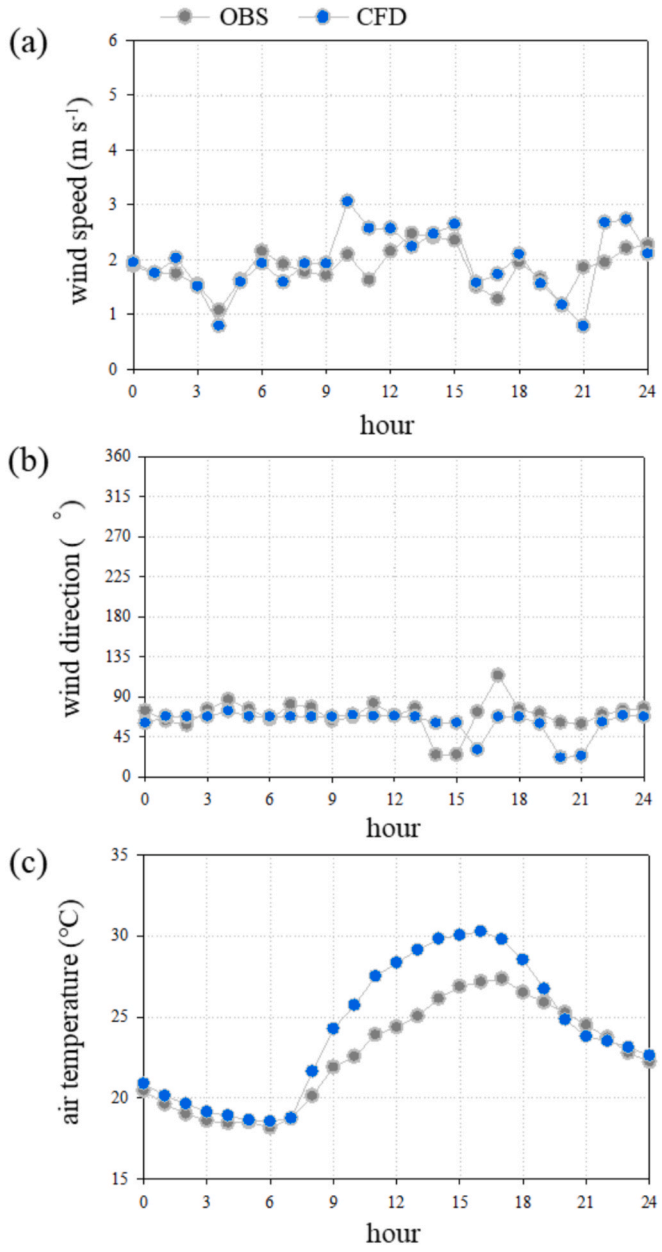

Fig. 5. Comparison of (a) wind speeds, (b) wind directions, and (c) air temperatures measured by Kim et al. [107] (grey symbols) and simulated by the CFD model (blue symbols) at 7 m above the rooftop of B3, from 00:00 to 24:00 LST (local standard time) on 7 September 2015. (For interpretation of the references to colour in this figure legend, the reader is referred to the web version of this article.)

staggered grid system. To ensure physically consistent thermal forcing at urban surfaces, the CFD model applies surface-temperature boundary conditions derived from the energy balance computed by the CitySim

Table 5
Statistical evaluation of meteorological variables (wind speed, wind direction, and air temperature) simulated by the CFD model. Values in square brackets denote the performance benchmarks suggested by Gavidia-Calderón et al. [108].

	wind speed [criteria]		wind direction [criteria]		air temperature [criteria]	
|MB|	0.1 m s^{-1}	[< 1.5 m s^{-1}]	8.2 °	[< 10 °]	1.45℃	[< 1.0℃]
RMSE	0.43 m s^{-1}	[< 2.5 m s^{-1}]	–		–	
MAE	–		15.7 °	[< 55 °]	1.56℃	[< 3.0℃]
IOA	–		–		0.92	[≥ 0.8]

Pro model. Although some CFD frameworks incorporate integrated solar radiation modules, this coupling strategy was adopted to explicitly account for the thermal inertia of multi-layered building assemblies and longwave radiative trapping between urban surfaces—physical processes that are often oversimplified in commonly used CFD solar radiation modules. By prescribing these physically derived surface temperatures, the CFD model resolves high-resolution airflow and heat advection driven by a realistic urban energy balance, rather than relying on simplified representations of solar heat gains. This approach builds upon established methodologies, such as the successful coupling of CitySim Pro with OpenFOAM and the Canopy Interface Model (CIM) for urban microclimate analysis [53,64]. Consequently, this framework allows for a more robust analysis of the near-surface thermal environment under the influence of advanced building envelope materials.

2.3. Numerical simulation set-up

2.3.1. Numerical domain

The target area is a high-density commercial district in Seoul, Republic of Korea, encompassing portions of Jongno-gu and Jung-gu (37.572° N, 126.978° E). At the domain center, a 70 m-wide north–south arterial road intersects with a 20 m-wide east–west street. Gwanghwamun Square—a major public space with high pedestrian activity—is located near the northern end of the domain. The surrounding high-rise buildings were oriented predominantly east–west, forming a street canyon (Fig. 2a). The urban morphology of the target area is characterized by a complex mixture of high-rise and low-rise buildings, resulting in pronounced spatial heterogeneity. Gwanghwamun Square, which constitutes the core of the numerical domain, exhibits the characteristics of an open space (hereafter, denoted as OSD; A in Fig. 2b). In addition, the built-up area is composed of several urban typologies: a district dominated by densely clustered high-rise buildings (dense high-rise district, DHD; B in Fig. 2b); low-rise areas surrounded by high-rise buildings and influenced by radiative shielding effects (sheltered low-rise district, SLD; C in Fig. 2b); and low-rise districts where high-rise buildings are relatively distant (dense low-rise district, DLD; D in Fig. 2b). In densely built or sheltered areas (DHD and SLD), multiple reflections between building surfaces and longwave radiative trapping are pronounced, and air stagnation is likely to occur. In contrast, the OSD is directly exposed to solar radiation during the daytime, making it more sensitive to the shortwave reflection effects induced by cool-coating applications. In this study, the analysis focuses on these representative areas to elucidate how urban morphology governs surface and thermal responses. The domain contains no water bodies; while street trees exist along certain road segments, vegetation effects were not explicitly represented in the present simulations to isolate the physical impacts of surface cool coatings. This limitation and the potential for integrated analysis with greenery are further discussed in Section 4. The computational domain measures 948 m × 948 m × 1004.2 m in the x, y, and z directions, respectively. Uniform grids with a spacing of 3 m were applied in the x and y directions, while a vertically stretched grid (stretching ratio of 1.1) was employed in the z direction, with a maximum cell size of 32.5 m. Building geometries were constructed based on GIS data provided by the National Geographic Information Institute of Korea (Fig. 2c). The lateral boundaries were placed at a distance of $10H_{max}$ from the built-up area (where H denotes building height and H_{max} = 160 m), and the top boundary at $5H_{max}$, in accordance with COST Action 732 guidelines [65]. To justify the selected grid resolution, a grid sensitivity analysis was performed by comparing coarse (6 m), medium (3 m), and fine (1.5 m) meshes. The results confirmed that the 3 m grid spacing strikes an optimal balance between computational efficiency and numerical accuracy. The selected resolution exhibited consistent flow and thermal patterns compared to the fine mesh, justifying its utilization for the primary simulations (Fig. S1).

2.3.2. Physical properties of buildings

To perform simulations with the CitySim Pro model, the physical properties of buildings and ground surfaces were specified; the configurations adopted in this study are summarized in Table 1. Here, constructions refer to multi-layer assemblies of the building facade and ground surface, in which each layer is characterized by thickness, thermal conductivity, density, and specific heat capacity [66]. Because accurately capturing the highly diverse compositions of all buildings is impractical, a uniform configuration was applied across all building facades and ground surfaces. However, for building facades, aluminum panels are commonly used in high-rise buildings but rarely in low-rise buildings. Therefore, for buildings ≤ 30 m in height, facades were assumed to be finished with ceramic tiles, while roof- and ground-surfaces were composed of concrete tiles and asphalt, respectively.

The thermal transmittance of building envelopes varies with insulation thickness, which is determined according to construction-year-specific standards. In this study, the composites for each construction year were assigned based on the standards provided by Adilkhanova et al. [67]. Because thermal transmittance represents the amount of heat transferred per unit area and time, a lower value indicates better insulation performance. Accordingly, the insulation thickness was adjusted to meet the thermal-transmittance criteria for each building. The final thermal-transmittance ranges were: walls, 2.09–0.27 $W•m^{-2}$ K^{-1}; roofs, 1.05–0.18 $W•m^{-2}$ K^{-1}; floors, 1.74–0.29 $W•m^{-2}$ K^{-1}; windows, 4.19–2.1 $W•m^{-2}$ K^{-1}. Other parameters followed Adilkhanova et al. [67], who examined a comparable high-density commercial district in Korea, including glazing ratio (0.30), solar-gain transmission (g-value = 0.70), operable-window fraction (0.10), infiltration rate (0.20 h^{-1}), and occupancy density (7 m^2 per person).

2.3.3. Scenarios with cool coating materials

The temperature of building facades and ground surfaces is strongly influenced by the radiative properties of exterior materials—namely solar reflectance (shortwave) and longwave emissivity. High solar reflectance reduces absorption of incoming radiation, while high emissivity enhances thermal emission; both contribute to surface cooling. However, in dense urban street canyons, highly reflective surfaces may also increase the temperatures of adjacent surfaces through multiple reflections [68,69]. It is therefore essential to evaluate how material radiative and thermal properties affect surface and air temperatures as well as outdoor thermal comfort in complex urban settings.

In the target area, exterior materials such as aluminum panels (high-rise building facade), ceramic tiles (low-rise building facade), concrete tiles (roof surfaces), and asphalt (ground surfaces) are predominant (Table 1). The control experiment (CNTL) adopted representative radiative properties for these materials:

– High-rise building facades (height ≥ 30 m): reflectance = 0.78, emissivity = 0.03.
– Low-rise building facades (height < 30 m): reflectance = 0.60, emissivity = 0.90.
– Roof surfaces: reflectance = 0.55, emissivity = 0.63.
– Ground surfaces: reflectance = 0.20, emissivity = 0.90.

Because building-specific facade data were unavailable—and optical

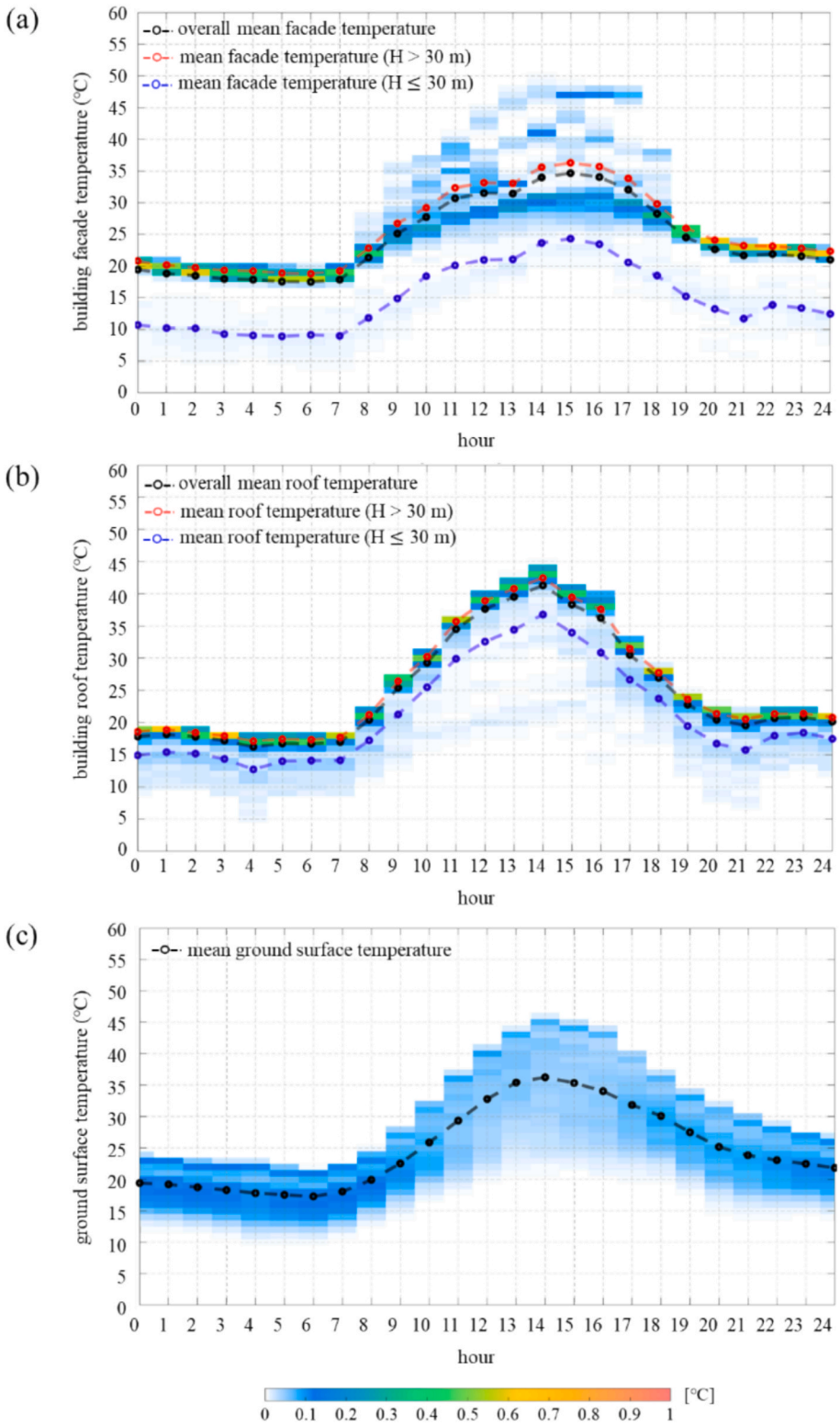

Fig. 6. Heatmaps showing the diurnal frequency distributions of (a) building facade, (b) roof, and (c) ground surface temperatures in control experiment (CNTL) from 00:00 to 24:00 LST (local standard time) on 7 September 2015. Black scatter lines indicate the domain-mean surface temperatures. Red and blue scatter lines in Fig. 6a and 6b represent the mean surface temperatures of high-rise and low-rise buildings, respectively. (For interpretation of the references to colour in this figure legend, the reader is referred to the web version of this article.)

properties vary with aging, oxidation, color, and finish—the reflectance–emissivity pairs were selected within literature-reported ranges and calibrated against observed surface temperatures (Section 3) [70–77].

Cool-coating materials—such as ceramic coatings and highly reflective paints—are widely recognized as cost-effective options for simultaneously increasing reflectance and emissivity without major reconstruction [24,39,78–82]. Recent studies also suggests that the reflective roofs exert limited influence on near-ground air temperature

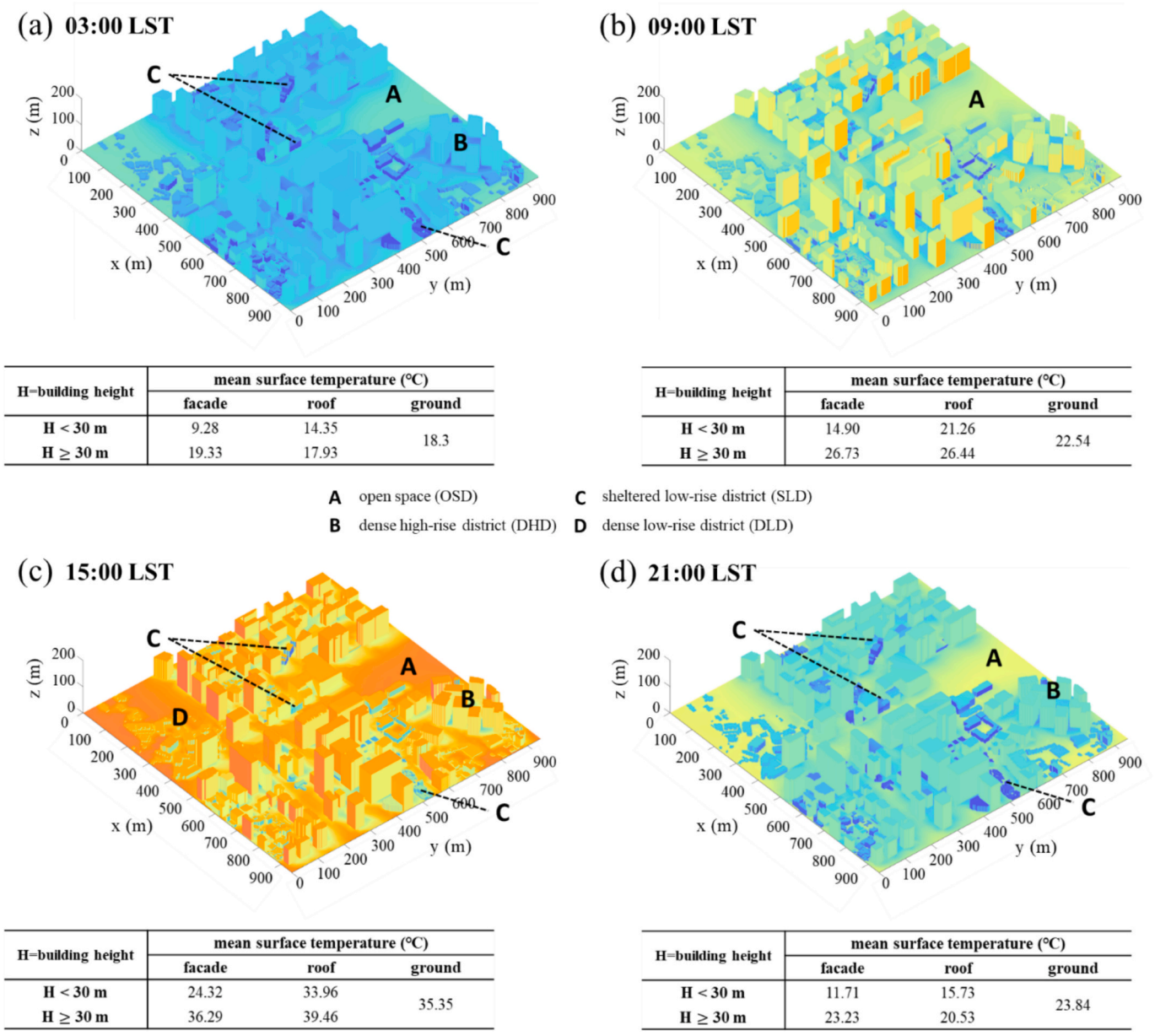

H=building height	mean surface temperature (°C)		
	facade	roof	ground
H < 30 m	9.28	14.35	18.3
H ≥ 30 m	19.33	17.93	

H=building height	mean surface temperature (°C)		
	facade	roof	ground
H < 30 m	14.90	21.26	22.54
H ≥ 30 m	26.73	26.44	

H=building height	mean surface temperature (°C)		
	facade	roof	ground
H < 30 m	24.32	33.96	35.35
H ≥ 30 m	36.29	39.46	

H=building height	mean surface temperature (°C)		
	facade	roof	ground
H < 30 m	11.71	15.73	23.84
H ≥ 30 m	23.23	20.53	

Fig.7. Three-dimensional distributions of building facade and ground surface temperatures in control experiment (CNTL) at (a) 03:00, (b) 09:00, (c) 15:00, and (d) 21:00 LST (local standard time) on 7 September 2015. Annotations A, B, C, and D indicate the open space (OSD), dense high-rise (DHD), sheltered low-rise (SLD), and dense low-rise districts (DLD), respectively.

in high-rise districts [24,83]. Typical properties are reflectance 0.80–0.90 and emissivity ≈ 0.90 for ceramic coatings [84], while cool-paint reflectance varies by color but generally be set to ≥ 0.8 for facades and ≥ 0.5 for asphalt pavements [81,85]. In this study, coatings were assumed to be applied directly over existing surfaces—ceramic coatings on high-rise facades and cool paints on low-rise facades and ground surfaces. Adopted thermal conductivity, density, specific heat capacity, and layer thickness for each coating are summarized in Table 2 [86,87]. After coating, the radiative properties were modified as follows:

– High-rise building facades: reflectance increased from 0.80 to 0.90, emissivity from 0.03 to 0.90.

– Low-rise building facades: reflectance from 0.60 to 0.80, emissivity ≈ 0.90.

– Ground surfaces: reflectance from 0.20 to 0.50, emissivity ≈ 0.90.

Because the thermal-property ranges of ceramic coatings and cool paints largely overlap, identical wall properties were assigned in all scenarios (reflectance 0.80–0.90, emissivity 0.90) Reflectance levels for building facades and ground surfaces were varied in 0.05 increments within their respective ranges for sensitivity experiments. Moreover, roof-coating scenarios excluded because of their minimal influence on pedestrian height air temperature [24,83].

To assess how modified surface properties of buildings and ground surfaces affect the urban thermal environment—following cool coating application especially in high-rise, high-density districts—influence the urban microclimate in districts with heterogeneous building heights, a total of 15 sensitivity experiments were conducted (Table 3). In all sensitivity experiments, the longwave emissivity of the cool-coated surfaces was fixed at 0.90 [16,67,75,88,89]. Meanwhile, the reflectance was varied at three levels for building facades (0.8, 0.85, 0.9) and ground surfaces (0.50, 0.55, 0.60). As illustrated in Fig. 3, which provides a spatial visualization of the surface property modifications, these experiments were categorized into three groups: ground-only, facade-only, and combined cool-coating applications.

1) BiGc — facade-only: building-facade reflectance varied (ground

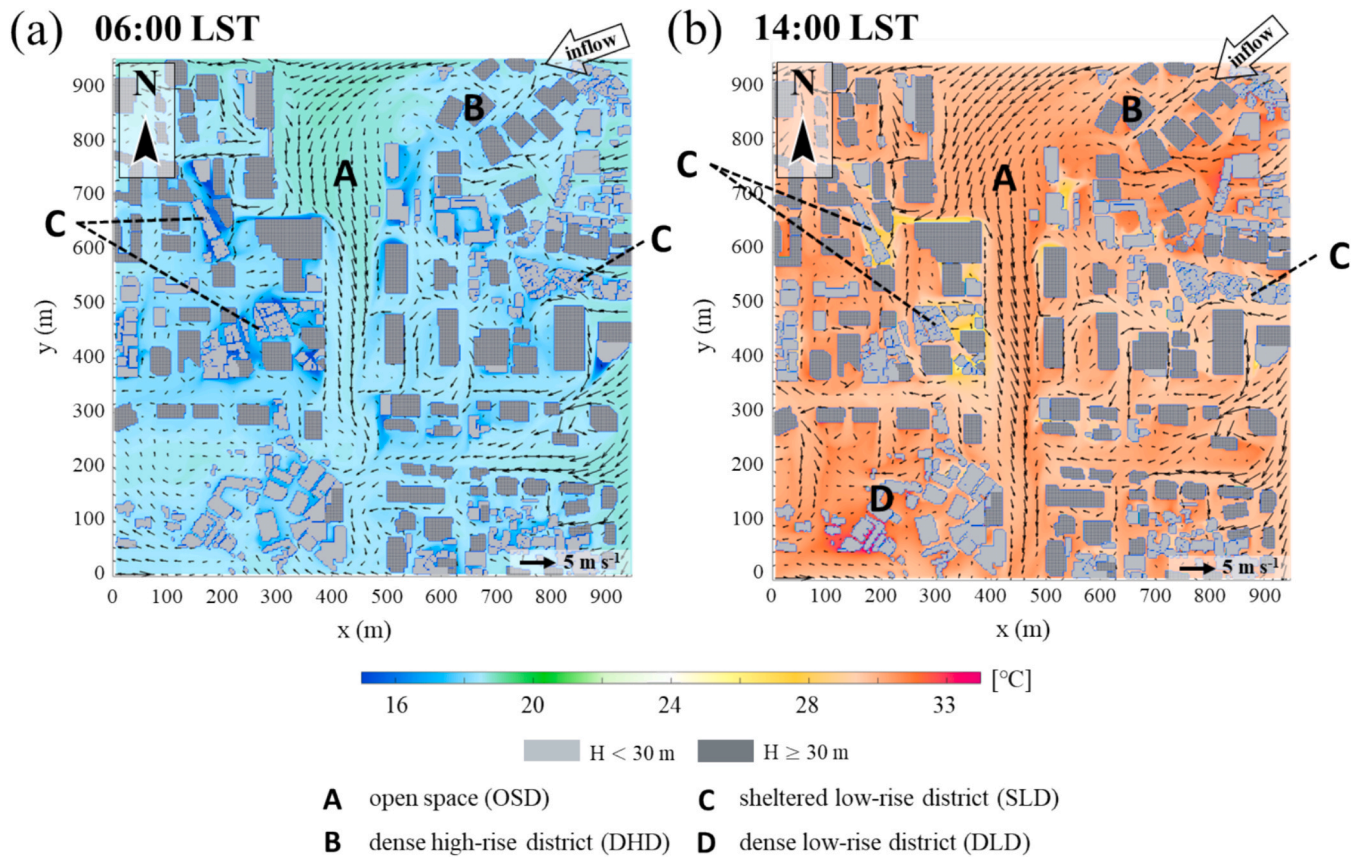

Fig. 8. Wind vectors, streamlines and air temperature contours at the pedestrian height (1.5 m) at (a) 06:00 and (b) 14:00 LST (local standard time) on September 7, 2015 in control experiment (CNTL). Light grey shading indicates buildings lower than 30 m, while dark grey represents buildings higher than 30 m. Annotations A, B, C, and D indicate the open space (OSD), dense high-rise (DHD), sheltered low-rise (SLD), and dense low-rise districts (DLD), respectively.

Table 6
Daily mean surface temperature difference of sensitivity experiments compared with CNTL.

Sensitivity experiments	Building facade		Building roof		Ground surface
	Low-rise	**High-rise**	**Low-rise**	**High-rise**	
B1Gc	6.01	−4.70	4.03	1.02	4.82
B2Gc	5.73	−5.06	3.98	1.02	4.82
B3Gc	5.43	−5.43	3.93	1.01	4.83
BcG1	0.21	0.37	0.07	0.01	−1.71
BcG2	0.25	0.44	0.08	0.01	−1.98
BcG3	0.28	0.50	0.09	0.01	−2.24
B1G1	6.02	−4.68	4.05	1.02	3.33
B1G2	6.02	−4.68	4.06	1.02	3.06
B1G3	6.03	−4.68	4.06	1.02	2.79
B2G1	5.69	−5.10	3.99	1.02	3.32
B2G2	5.68	−5.10	4.00	1.02	3.05
B2G3	5.67	−5.11	4.00	1.02	2.78
B3G1	5.34	−5.52	3.93	1.02	3.31
B3G2	5.32	−5.54	3.93	1.02	3.04
B3G3	5.30	−5.56	3.93	1.02	2.76

fixed at CNTL; i = 1, 2, 3 denote reflectance level).

2) BcGj — ground-only: ground-surface reflectance varied (j = 1, 2, 3 denote reflectance level);

3) BiGj — combined: both facade and ground reflectance varied simultaneously (i, j = 1, 2, 3).

While aging and soiling can reduce the reflectance of cool materials to a certain level, the scenarios considered in this study encompass the variation ranges of reflectance, emissivity, and surface temperature resulting from these factors, based on the additional sensitivity experiment results (Fig. S2) and previous literature [90–95].

Surface temperature were first predicted by the CitySim Pro model and then used as boundary inputs in the CFD model to evaluate the resulting changes in surface-air interactions and the pedestrian height thermal environment.

2.3.4. *Meteorological data and boundary condition*

Hourly meteorological data from Automated Synoptic Observation System (ASOS 108) operated by the Korea Meteorological Administration (KMA) were used to provide boundary conditions for the coupled CFD-CitySim Pro model. ASOS 108, located approximately 950 m west of the target area, supplied observations of air temperature (T_a), ground temperature (T_g), relative humidity (RH), wind speed and direction, precipitation, and cloud cover to drive CitySim Pro's prediction of building and ground surface temperatures. For solar radiation inputs, diffuse horizontal irradiance (GDh) and direct beam normal irradiance (GBn) were obtained from the Photovoltaic Geographical Information System (PVGIS) of the Joint Research Centre (JRC) of the European Union. The PVGIS dataset provides hourly solar radiation data at 0.28° spatial resolution, derived from ERA5 reanalysis [96]. Numerical simulations were conducted for a 24-hour period (00:00 LST to 24:00 LST) on 7 September 2015, under clear-sky conditions. On this site, the mean air temperature was 25.4℃ (maximum 31.2℃, minimum 19.9℃), and the mean wind speed was 2.24 m s^{-1}, with predominantly northeasterly winds. To ensure the climatic robustness of the study, the long-term meteorological characteristics of the target area were analyzed using ASOS 108 data for August–September during 2010–2020 (Fig. S3). During this decadal period, the area exhibited warm conditions with distinct diurnal temperature ranges. The median air temperature typically fluctuated between 22℃ and 28℃; while strong winds occurred

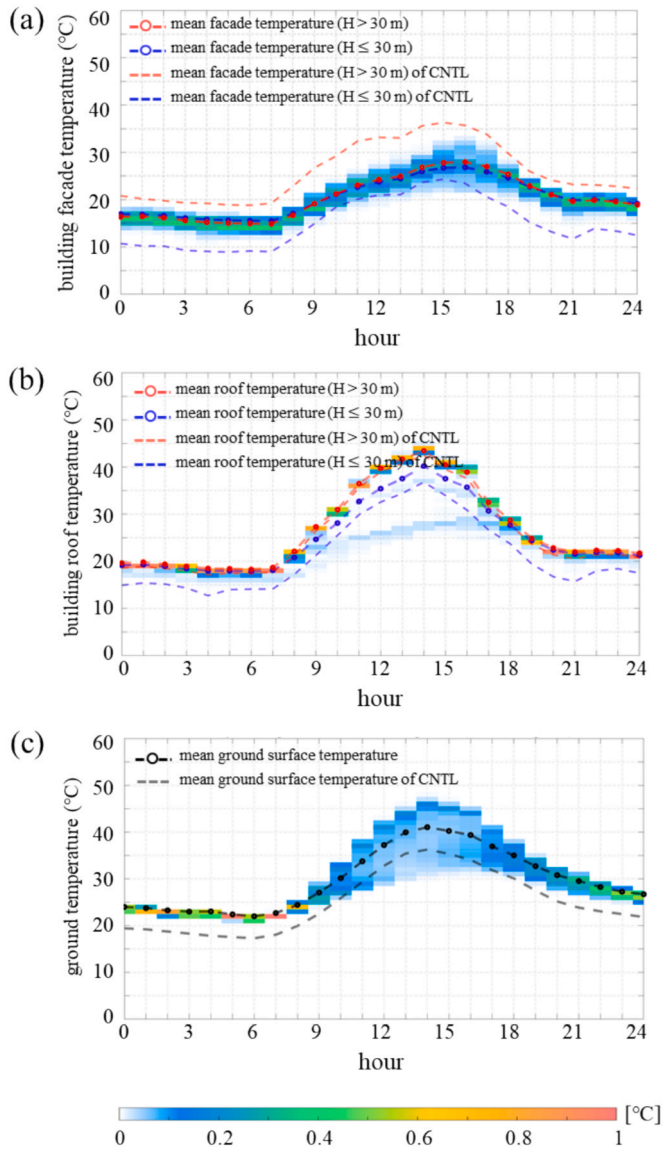

Fig. 9. The same as Fig. 6 except for B3Gc.

intermittently, weak winds below 3 m s^{-1} were predominant. A comparison of the target date against these long-term statistics revealed that both air temperature and wind speed remained well within the typical decadal climatic trends. Consequently, the selected target date is considered a representative period for analyzing the urban microclimate of the late-summer season in Seoul.

Hourly 10-m wind speed and direction and 2-m air temperature measured at ASOS 108 were used to construct hourly time-varying vertical inflow profiles of wind velocity components (U, V, W) and air temperature (T_a). These profiles assume an inflow boundary-layer condition, with the inflow direction kept vertically uniform across the inlet. The simulation was performed by updating the inflow boundary conditions at hourly intervals to reflect the measured wind direction changes, ensuring that the transient nature of the urban microclimate was captured.

$$U = \frac{U_*}{\kappa}\ln\left(\frac{z}{z_0}\right)cos\theta, \tag{1}$$

$$V = \frac{U_*}{\kappa}\ln\left(\frac{z}{z_0}\right)sin\theta, \tag{2}$$

$$W = 0, \tag{3}$$

$$T_a = T_{ref} - \Gamma(z - z_{ref}). \tag{4}$$

Here, U_* denotes the friction velocity; z_0 is the roughness length (0.05 m); θ represents the wind direction; T_{ref} is the air temperature at the reference height; and Γ is the environmental lapse rate (−6.5 K km^{-1}). The turbulent kinetic energy (TKE, k), and TKE dissipation rate (ε) at the inflow boundary were specified as follows [97]:

$$k = \frac{1}{C_\mu^{0.5}}U_*^2\left(1 - \frac{z}{\delta}\right)^2, \tag{5}$$

$$\varepsilon = \frac{C_\mu^{0.75}k^{1.5}}{\kappa z}. \tag{6}$$

Here, δ is the boundary-layer depth (1000 m) and κ is the von Kármán constant (0.4). Building-facade and ground-surface temperatures predicted by the CitySim Pro model were prescribed as hourly boundary conditions in the CFD model. A zero-gradient boundary condition was applied at the outflow, lateral, and top boundaries, and turbulent flow near solid walls was represented using the wall functions of Versteeg and Malalasekera [98].

2.4. Universal thermal climate index (UTCI)

In this study, the Universal Thermal Climate Index (UTCI) was employed to evaluate outdoor pedestrian thermal comfort in response to changes in the radiative properties of building facades and ground surfaces. The UTCI is standardized local index for assessing human thermal comfort by jointly accounting for air temperature, wind speed, relative humidity, mean radiant temperature (T_{mrt}), and human thermophysiological response [99–106] The UTCI was computed using the UTCI-Fiala operational procedure [99]. Calculations were performed under standard reference assumptions, including an activity level equivalent to walking at 4 km h^{-1} (≈ 2.3 MET), while incorporating the UTCI adaptive clothing model to reflect realistic outdoor thermal adaptation.

$$UTCI = T_a + Offset(T_a, ws_a, RH, \Delta T_{mrt}) \tag{7}$$

$$P_a = \frac{RH}{100}e_s(T_a) \tag{8}$$

$$e_s(T_a) = 6.211\exp\left(\frac{17.62T_a}{243.12 + T_a}\right) \tag{9}$$

Where e_s is the saturation vapor pressure. Especially under summer daytime conditions with direct solar radiation, UTCI responds sensitively to changes in the radiative environment.

In this study, UTCI was calculated along the central walkway of Gwanghwamun Square (indicated by the red line in Fig. S4)—a high-foot-traffic open space—to evaluate outdoor thermal comfort. The T_{mrt} values for the UTCI calculation were derived from the CitySim Pro model, while air temperature and wind speed were extracted from the CFD model at the same spatial coordinates. Relative humidity was based on field measurements, which served as input for the CitySim Pro simulations. To ensure high-resolution assessment while minimizing radiative interference between modeled individuals, pedestrians were positioned at 3 m intervals along the walkway in the CitySim Pro T_{mrt} calculations. The UTCI values obtained along the central walkway were averaged for the analysis. Furthermore, the results of the sensitivity analysis regarding T_{mrt} uncertainty (Fig. S5) indicate that the impact of potential T_{mrt} fluctuations on the variability of UTCI thermal stress categories is relatively limited, confirming the robustness of the comfort assessment.

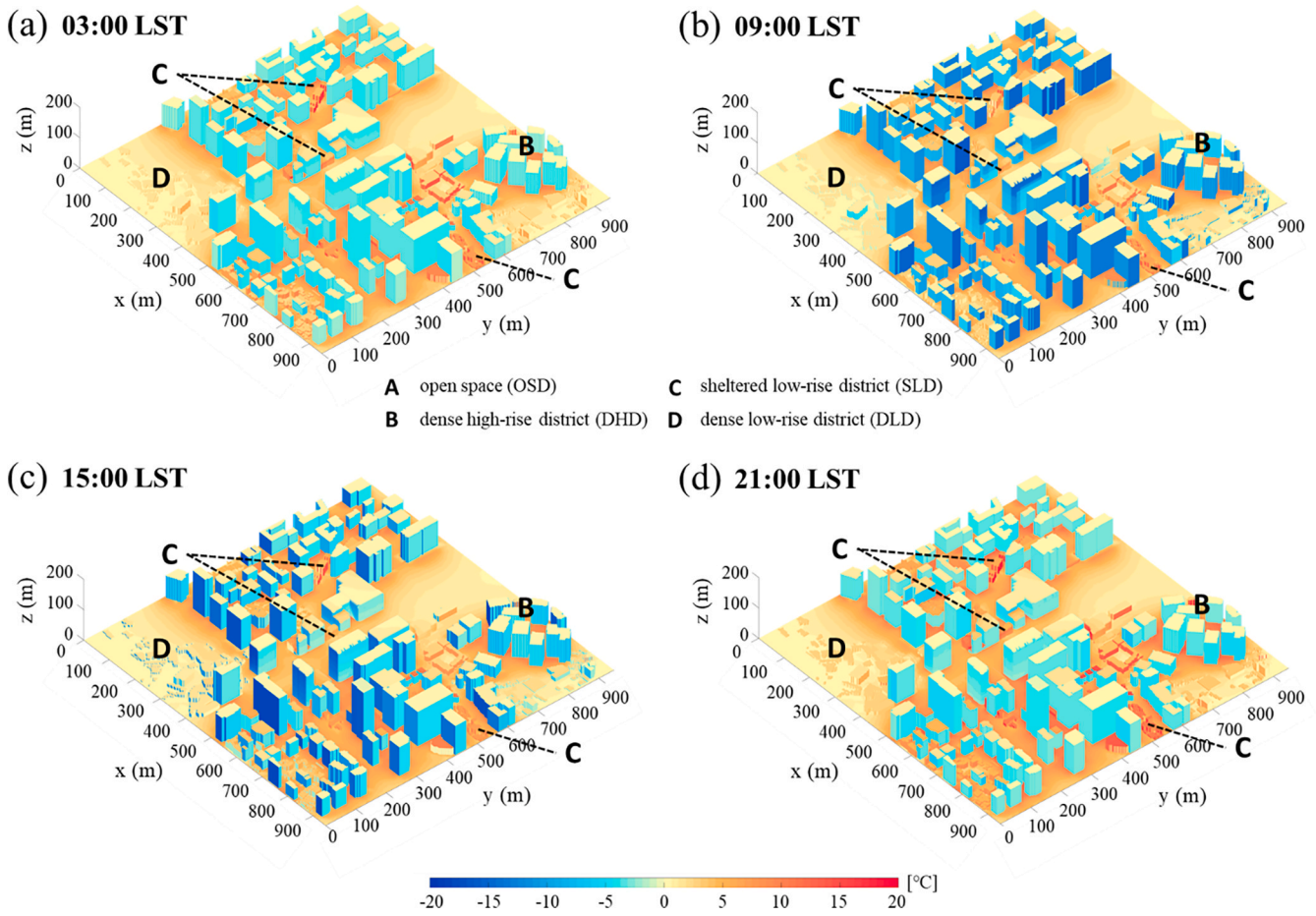

Fig. 10. Three-dimensional distributions of surface temperature differences between B3Gc and control experiment (CNTL) at (a) 03:00 LST (local standard time), (b) 09:00 LST, (c) 15:00 LST, and (d) 21:00 LST on 7 September 2015. Annotations A, B, C, and D indicate the open space (OSD), dense high-rise (DHD), sheltered low-rise (SLD), and dense low-rise districts (DLD), respectively.

3. Results and discussion

3.1. Control experiment (CNTL)

3.1.1. Numerical model validation

To evaluate the prediction accuracy of the CitySim Pro and CFD models, simulation results were compared with field measurements conducted by Kim et al. [107] on 7 September 2015. Observations included building-facade, rooftop, and ground-surface temperatures, as well as wind speed, wind direction, and air temperature measured 7 m above the rooftop of B3. Infrared camera data were collected at building facades (① and ② on B1 and ③ on B2), rooftops (④ on B3), and the ground (⑤) (Fig. 2c). Except for the consistently shaded facade ② on B1, maximum surface temperatures approached 40℃ (Fig. 4). East-facing facades (① on B1 and ③ on B2) warmed steadily in the morning under direct solar radiation and cooled in the afternoon, whereas the shaded facade (② on B1), rooftop (④ on B3), and ground surface (⑤) reached their peak temperatures in the afternoon. The CitySim Pro model reproduced these diurnal temperature variations well (Fig. 4). Quantitatively, the predictions demonstrated high accuracy, as summarized in Table 4. Across all monitored sites—including vertical facades and horizontal surfaces—the results showed strong agreement with observations, with RMSE values ranging from 1.62℃ to 2.37℃ and both R^2 and IOA exceeding 0.8. These results confirm the model's reliability and indicate that the thermal-property parameters used in CNTL were well calibrated. In CNTL, CitySim Pro surface temperatures were prescribed as boundary conditions for the CFD model. Comparisons with meteorological observations (Fig. 5) showed that: (1) wind speeds generally followed observed trends despite slight overestimation; (2) wind direction was predominantly northeasterly, with simulated patterns aligning well with measurements; and (3) air temperatures matched nighttime observations closely, with a modest daytime overestimation. Following the performance benchmarks by Gavidia-Calderón et al. [108], all results in this study satisfied the criteria, confirming the model's reliability (Table 5).

Overall, these validation results demonstrate that both the CitySim Pro and the CFD models accurately reproduce key features of urban microclimate—surface temperatures, airflow, and air temperature—confirming that the building–ground composite configuration, specified surface reflectance and longwave emissivity, and radiative and meteorological boundary conditions were realistically represented. Since the validation is specific to the target period, further validation may be necessary under significantly different meteorological conditions or updated urban morphologies. Nonetheless, within this validated framework, the coupled modeling approach provides a robust foundation for analyzing how cool-coating material properties influence the thermal environment at the pedestrian height.

3.1.2. Effects of surface radiative properties on surface temperature and the pedestrian height microclimate

In CNTL, surface temperature fields were analyzed to identify distinct thermal behaviors categorized by building scale and orientation (Fig. 6). For low-rise buildings ($H < 30$ m), the daily mean surface temperatures for facades and roofs were 14.96℃ and 21.34℃, respectively. In contrast, high-rise buildings ($H \geq 30$ m) exhibited significantly higher thermal levels, with daily mean facade and roof temperatures of

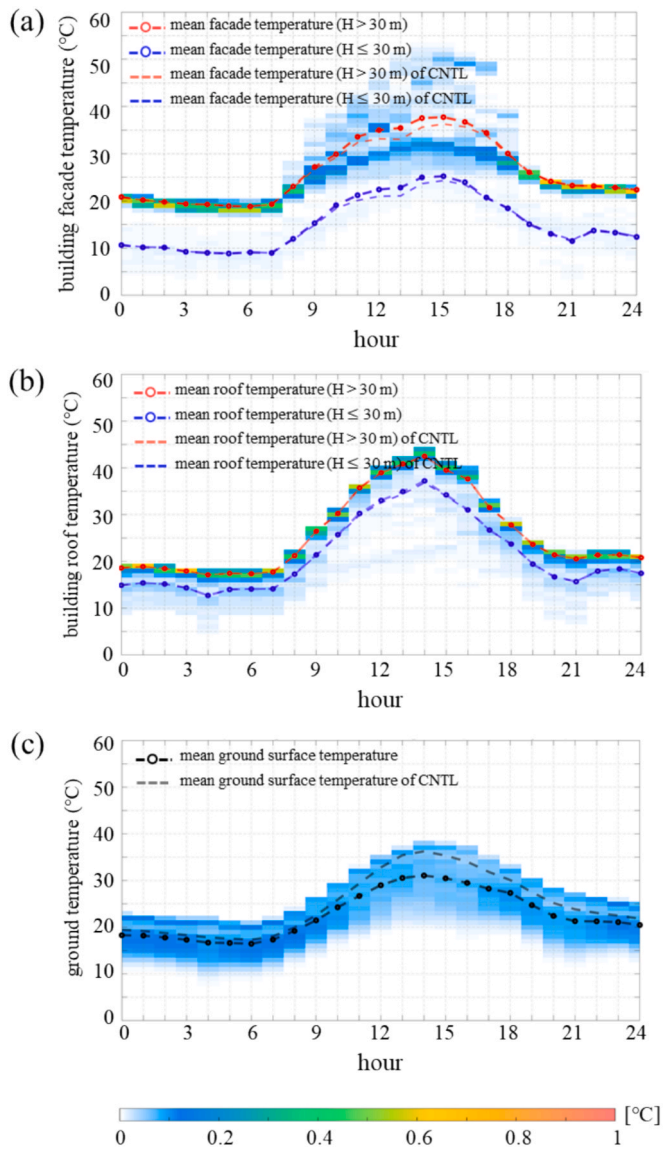

Fig. 11. The same as Fig. 6 except for BcG3.

25.85℃ and 25.79℃, respectively. These findings highlight substantial thermal disparities driven by building materials. Specifically, high-rise facades, characterized by low longwave emissivity (0.03), exhibited a mean surface temperature approximately 10.89℃ higher than those of low-rise facades (0.90). The daily mean ground surface temperature was 24.95℃.

Mean surface temperatures for both building facades and the ground were lowest at 06:00 LST and peaked between 14:00 LST and 15:00 LST (Fig. 6a and c). Rooftop surfaces reached their daily minimum and maximum at 04:00 LST and 14:00 LST, respectively (Fig. 6b). Generally, rooftops exhibit higher temperatures than facades due to the direct solar exposure, a trend particularly pronounced in low-rise buildings. Spatial variability was greater on building facades than on the ground. During the early morning (00:00–07:00 LST), building facade temperatures ranged from 18℃ to 23℃ under radiative cooling (Fig. 6a). From 08:00–13:00 LST, facade temperatures rose with increasing solar radiation, subsequently decreasing from 14:00–18:00 LST as solar input declined. During the daytime, sunlit facades warmed rapidly while shaded facades warmed more moderately, yielding greater spatial thermal contrasts than those observed at night. At night (19:00–24:00 LST), facade temperatures remained approximately 5℃ higher than in the early morning because of daytime heat storage [109,110]. A similar diurnal trend was observed for roof temperatures, which were primarily governed by solar irradiance during the day and exhibited sustained nocturnal warmth due to heat storage (Fig. 6b). Ground surface temperatures ranged between 13 and 25℃ from 00:00 to 07:00 LST, then increased sharply under solar heating to reach a peak of approximately 46℃ at 14:00 LST (Fig. 6c). Between 15:00 and 18:00 LST, temperatures decreased as solar radiation weakened. Daytime shading substantially modulated ground surface temperatures, producing stronger spatial heterogeneity compared to nocturnal conditions. Between 19:00 and 24:00 LST, ground surface temperatures remained between 15℃ and 36℃, consistent with sustained warmth resulting from daytime heat accumulation.

Diurnal evolution of surface temperatures reflected the synergistic effects of envelope radiative properties, solar altitude/azimuth, and urban shading (Fig. 7). Specifically, the three-dimensional spatial distribution clearly illustrates pronounced disparities in thermal patterns among the categorized urban typologies. At 03:00 LST, when radiative cooling dominated the energy balance, high-rise facades exhibited the highest mean surface temperature (19.33℃), exceeding low-rise facades (9.28℃). In contrast, high-rise roofs (17.93℃) were slightly cooler than the ground (18.30℃) but warmer than low-rise roofs (14.35℃). This discrepancy is primarily because high-rise facades in the DHD (B in Fig. 7a) possess an exceptionally low longwave emissivity, which inhibits radiative cooling. In contrast, surface temperatures in the SLD (C in Fig. 7a) remain significantly lower, as their high longwave emissivity allows for more efficient nocturnal cooling. In the OSD (A in Fig. 7a), the ground temperature remained warmer than in the densely built surroundings, indicating a significant carryover of daytime heat. By 09:00 LST, surface temperatures rose with increasing solar irradiance. The mean temperatures of high-rise facades (26.73℃) and roofs (26.44℃)—characterized by higher thermal conductivity (160 $W \cdot m^{-1} \cdot K^{-1}$)—exceeded those of low-rise facades (14.90℃) and roofs (21.26℃) (Fig. 7b). For the ground, which possesses lower conductivity, the mean ground surface temperature in the OSD (A in Fig. 7b) reached approximately 29℃, surpassing the domain mean. At 15:00 LST, despite declining solar input, surface temperatures reached their daily maxima. Specifically, mean surface temperatures peaked at 36.29℃ for high-rise facades and 39.46℃ for roofs, while low-rise facades exhibited significantly cooler facades (24.32℃) and roofs (33.96℃). The elevated high-rise facade temperatures are attributable to low longwave emissivity and enhanced heat storage, whereas low-rise facades—with higher emissivity and lower conductivity—remained cooler. Notably, the DLD (D in Fig. 7c), which is relatively less influenced by shading from high-rise structures, exhibited slightly higher roof surface temperatures than the SLD (C in Fig. 7c), where radiative shielding and shading effects from adjacent high-rise buildings were more pronounced. In the OSD (A in Fig. 7c), ground surface temperatures were remarkably high due to the direct influence of solar radiation. By 21:00 LST, the mean low-rise facade temperature dropped to 11.71℃ (e.g., C in Fig. 7d) (the lowest among all facades), while high-rise facades remained significantly warmer at 23.23℃ (e.g., B in Fig. 7d). In the OSD (A in Fig. 7d), the ground temperature remained as high as 30℃, indicating a persistent influence of accumulated daytime heat that notably exceeded the overall mean ground temperature of 23.84℃. In contrast, the SLD (C in Fig. 7d), which benefited from earlier afternoon shading, demonstrated efficient nocturnal cooling, aligning with the inherently lower thermal levels of low-rise buildings.

Air temperature and wind fields at 1.5 m were examined for 06:00 and 14:00 LST, corresponding to the periods when surface temperatures were near their daily minimum and maximum, respectively (Fig. 8). At 06:00 LST, the inflow was east-northeast (70°), and wind corridors developed from the north and northwest into the OSD (A in Fig. 8a). The thermal environment at this hour was directly modulated by the nocturnal heat retention of the surrounding structures. Notably, stagnant zones with weak winds and limited ventilation were consistently observed within the densely built districts (e.g., B, C, and D in Fig. 8a). In

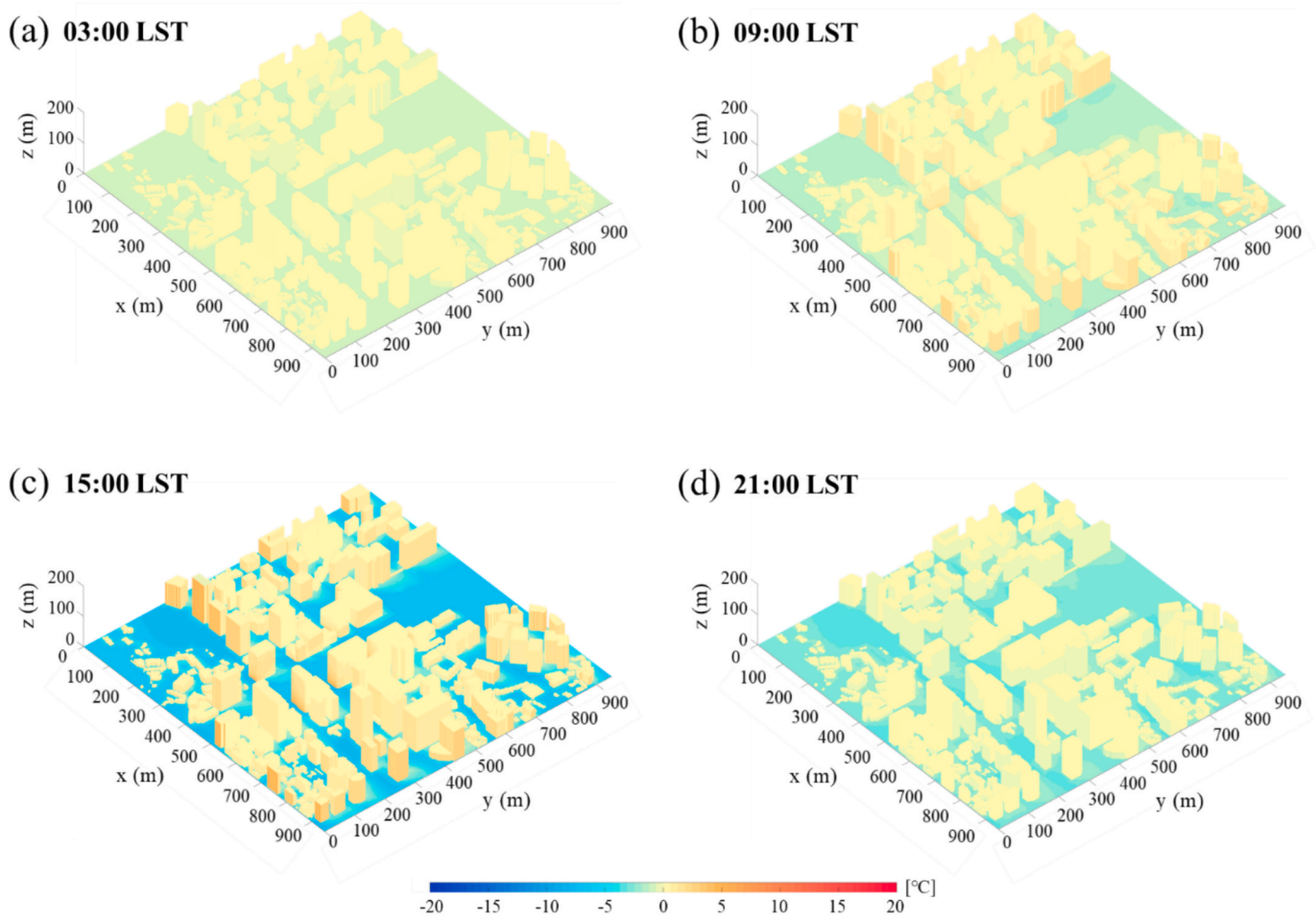

Fig. 12. The same as Fig. 10 except for BcG3.

the SLD (C in Fig. 8a), the lack of advection facilitated the formation of cold-air pools, directly reflecting the efficient nocturnal cooling of high-emissivity surfaces. Conversely, in the DHD (B in Fig. 8a), the stagnant air acted as a thermal buffer that trapped heat near the low-emissivity high-rise facades, leading to relatively higher air temperatures compared to the adjacent low-rise districts. At 14:00 LST, the inflow veered to the northeast (50°) (Fig. 8b). The overall flow pattern resembled that at 06:00 LST, but stronger background winds intensified the wind corridors within the OSD (A in Fig. 8b), where direct solar exposure maximized localized thermal levels. In the DHD (B in Fig. 8b), high surface temperatures combined with warm advection elevated air temperatures in the surrounding vicinity. Conversely, the SLD (C in Fig. 8b) acted as a cool spot, as extensive shading from surrounding high-rises maintained lower surface temperatures. Notably, the DLD (D in Fig. 8b) emerged as a thermal hot spot. Although facade temperatures were relatively lower than those high-rise buildings, this district was less affected by shading than SLD, leading to higher roof temperatures. Given that building heights are predominantly below 10 m, the close vertical proximity between these heated roofs and the pedestrian height likely enhanced the sensitivity of air temperature to roof heating.

This suggests that in dense urban configurations, the absence of ventilation serves to couple the pedestrian-height air temperature more tightly to the scale-dependent radiative properties of the building and ground envelopes. Furthermore, these results demonstrate that in morphologically complex districts, the pedestrian-height thermal environment is governed by the solar exposure of building facades and ground surfaces, as well as their geometric proportions. Additionally, surface-temperature contrasts—arising from building envelope material properties—directly modulate the near-surface air temperature field through localized heat exchange.

3.2. *Sensitivity experiments to radiative properties of cool-coating materials*

3.2.1. *Impact of cool-coating-induced radiative property changes on surface temperatures*

Relative to CNTL, we analyzed the differences in daily mean surface temperatures for building facades, roofs and the ground across all sensitivity experiments (Table 6). In BiGc (i = 1, 2, 3), high-rise facades cooled by 4.70–5.43℃ due to the synergistic effects of increased reflectance (daytime shortwave reduction) and higher longwave emissivity (enhanced nocturnal cooling). Conversely, although cool coatings were not applied to rooftop surfaces, high-rise roofs exhibited a slight temperature increase of approximately 1.0℃. This localized warming is attributed to the absorption of enhanced shortwave radiation reflected from the facades of adjacent, taller high-rise buildings. However, this magnitude remained smaller than that observed for low-rise roofs, as the higher sky view factors of high-rise roofs result in lower exposure to surrounding reflective surfaces. In contrast, adjacent low-rise facades and the ground warmed significantly due to the radiative burden imposed by intensified multiple shortwave reflections and enhanced longwave emissions from the high-rise facades. Consequently, low-rise building facades and roofs warmed by 5.43–6.01℃ and 3.93–4.03℃, respectively, while ground surfaces warmed by approximately 4.82℃. In BcGj (j = 1, 2, 3), the ground cooled by 1.71–2.24 ℃, whereas facades (< 0.5℃) and roofs (~0.1℃) showed only marginal warming due to

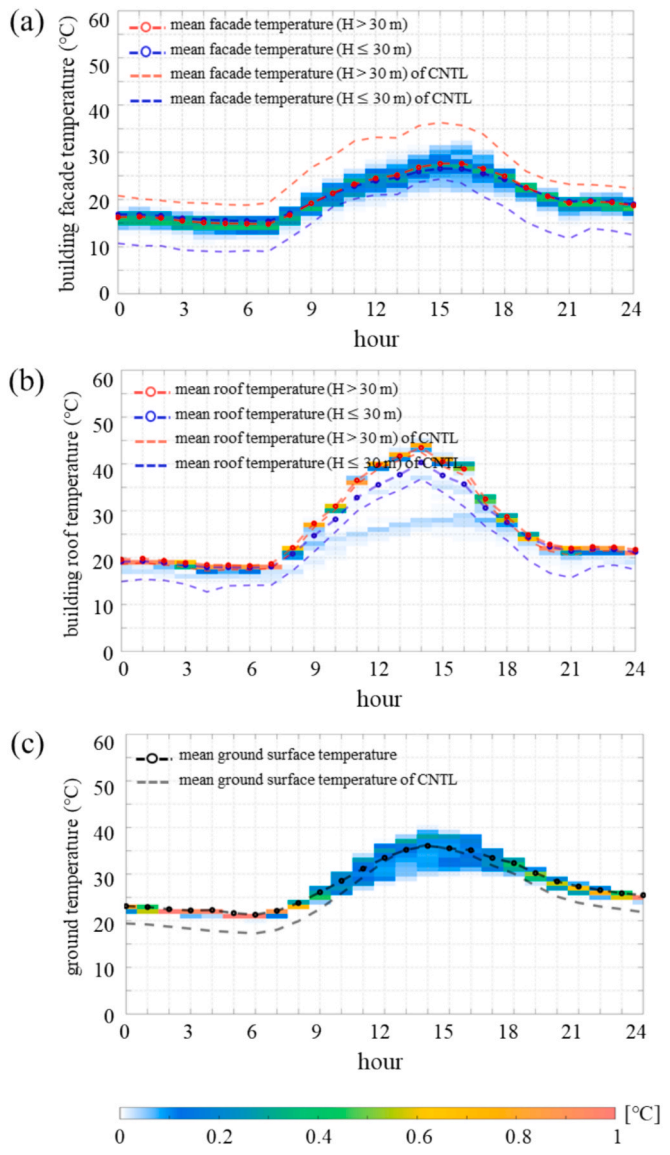

Fig. 13. The same as Fig. 6 except for B3G3.

upward reflection of shortwave radiation from the high-reflectance ground. In BiGj (i, j = 1, 2, 3), the trends resembled BiGc, but the concurrent increase in both facade and ground reflectance led to larger net cooling effect; for the ground, the relative warming seen in BiGc was reduced by up to ~ 2 ℃ in B3G3.

To investigate the mechanisms driving these thermal responses, an hourly analysis was conducted for the highest-reflectance cases (B3Gc, BcG3, and B3G3) (Figs. 9, 11 and 13). Across all experiments, facades, roofs and the ground exhibited minimum temperatures at 06:00–07:00 LST and maxima at 14:00–16:00 LST.

In B3Gc, high-rise facades showed significant cooling compared to CNTL, which was particularly pronounced during the daytime (08:00–18:00 LST) (Fig. 9a). This cooling is driven by the synergistic effects of increased solar reflectance and drastically enhanced longwave emissivity, which prevents heat accumulation despite the solar load. In contrast, low-rise facades exhibited warming, which was primarily observed during the nighttime (24:00–07:00 LST). This nocturnal warming is driven by the intensified longwave radiation emitted from the adjacent high-rise facades, whose emissivity increased drastically (from 0.03 to 0.90), thereby altering the canyon's radiative balance even in the absence of solar load. This height-dependent disparity extended to roof surfaces (Fig. 9b) with a different temporal pattern. While high-rise roofs showed only marginal temperature increases, low-rise roofs experienced a sharp thermal spike during the daytime, reaching temperatures 3.4℃ higher than CNTL at 14:00 LST. This confirms a distinct bifurcated heating mechanism: while low-rise facades were heated nocturnally by enhanced longwave emission, low-rise roofs were heated diurnally by absorbing the substantial shortwave radiative load reflected from the adjacent high-rise facades. This radiative burden further extended to the ground surface, which exhibited a consistent warming trend throughout the diurnal cycle (Fig. 9c). Driven by the combined effects of enhanced downwelling longwave radiation at night and intensified shortwave reflection during the day, the domain-mean ground temperature increased by approximately 4.83℃ (Table 6). The three-dimensional visualization of surface temperature differences further clarifies these height-dependent radiative trade-offs (Fig. 10). Consistent with Fig. 9, the cooling effect on high-rise facades (e.g., B in Fig. 10) was significantly more pronounced during the daytime than at night. Conversely, the SLD (C in Fig. 10) exhibited elevated surface temperatures throughout the diurnal cycle, which is attributable to radiative shielding and intensified longwave coupling from the surrounding high-rise buildings. In contrast, the DLD (D in Fig. 10), where high-rise buildings are distantly located, showed relatively lower surface temperatures than the SLD. This disparity arises because the DLD was less subjected to the redirected radiative burden from high-rise facades compared to the SLD. This spatial contrast visually confirms that the radiative energy removed from the cool-coated high-rise buildings is redistributed to the surrounding lower urban canopy.

In BcG3, the radiative interactions produced a distinct vertical contrast. While the ground surface exhibited significant cooling (Fig. 11c), adjacent building facades and roofs showed a reversal, characterized by slight warming exclusively confined to the daytime (Fig. 11a and b). This heating—averaging approximately 1℃—is driven by the upward reflection of shortwave radiation from the high-reflectance ground, which imposes an additional radiative load on the surrounding vertical surfaces. However, the resulting temperature increase of the building facades remained modest. Spatial distribution analysis corroborates this mechanism, showing warming hotspots across most building facades during peak solar hours (09:00 and 15:00 LST) (Fig. 12b and c). Notably, the ground surface exhibited its strongest cooling response at 15:00 LST, coinciding with peak solar irradiance (Fig. 12c), thereby maximizing the thermal contrast between the cooled ground and the slightly warmed buildings.

In B3G3, facade thermal patterns were similar to B3Gc, whereas the ground surface showed a marked difference due to the cool pavement application (Fig. 13). Unlike B3Gc, where the ground warmed, the presence of high-reflectance pavement in B3G3 successfully induced a net cooling effect. Specifically, at 15:00 LST, the ground temperature exhibited a distinct reduction compared to B3Gc, confirming that the direct radiative cooling from the ground cool coating was sufficiently robust to dominate the domain-scale thermal response, primarily driven by ground surface cooling (Fig. 14c).

3.2.2. *Spatial distribution of flow and air temperature*

Surface temperature anomalies were imprinted on the 1.5-m air temperature field, while wind patterns remained broadly similar to CNTL, indicating a geometry-controlled urban flow (Fig. 15). At 06:00 LST, high-rise facades in the DHD (B in Fig. 15a and 15c) reached lower surface temperatures in B3Gc and B3G3, resulting in localized air temperature reductions in their immediate vicinity. In contrast, B3Gc and B3G3 induced localized air temperature increases of 0.3–2.0℃, particularly within the OSD (A in Fig. 15a and 15c) and stagnation-prone districts (C and D in Fig. 15a and 15c). This nighttime warming was primarily driven by the redistribution of intensified longwave radiation from high-emissivity facades—a process further exacerbated by convective stagnation that inhibited effective heat dissipation. In contrast, BcG3 showed a slight nighttime cooling (< 0.5℃) across most areas, suggesting that ground-only modifications alleviate tropical-night

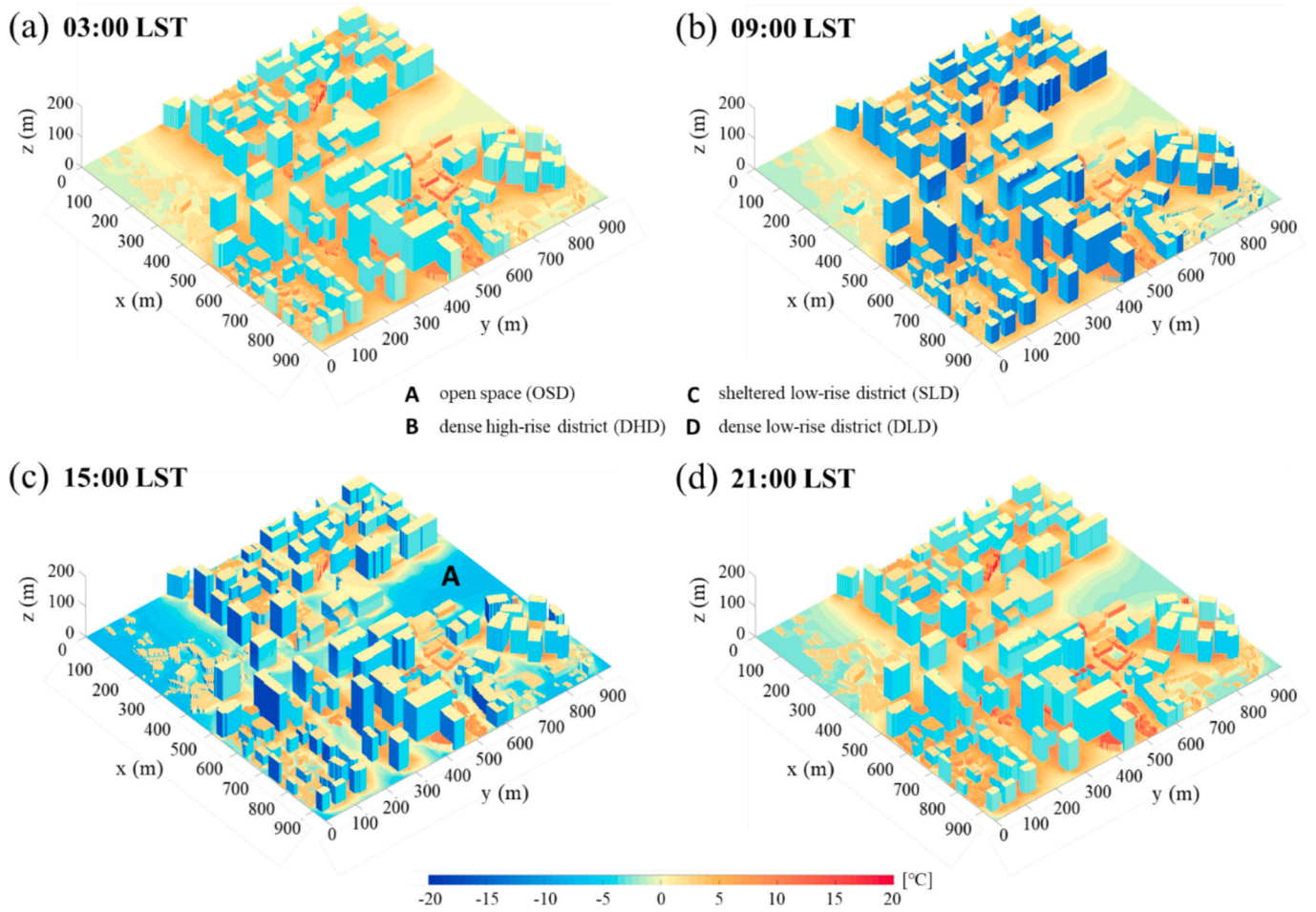

Fig. 14. The same as Fig. 10 except for B3G3.

conditions without imposing a nocturnal radiative burden (Fig. 15b). At 14:00 LST, intensified background winds enhanced the ventilation and the subsequent advection of cooling effect across the entire domain. In BcG3, cold inflow originating from the vicinity of the DHD (B in Fig. 15d) was effectively transported along the OSD (A in Fig. 15d), producing air temperature reductions of 0.4–1.0℃. This demonstrates that facade cool coatings can provide far-field thermal benefits when coupled with efficient ventilation corridors. In BcG3, radiative interactions produced a distinct spatial contrast: upward shortwave reflections from the high-reflectance ground generated localized warm pockets within some densely built areas, whereas in more open spaces with lower building density, the cooled ground surface led to a dominant reduction in air temperature. In B3G3, air temperature reductions extended over the widest area, confirming that the combined enhancement of facade and ground reflectance maximizes overall cooling efficacy.

Analysis of temporal deviations in domain-mean air temperature at pedestrian height revealed that ground-only cool coating scenarios (BcGj) generally exhibited slight temperature reductions, with the exception of a few specific hours. Conversely, scenarios incorporating facade cool coatings (BiGc and BiGj) showed a distinct diurnal trend, marked by slight temperature increases at night and decreases during the day. Notably, the reduction in daytime air temperature was maximized when both ground and facade coatings (BiGj) were applied (Fig. S6).

In a high-density urban district, these results demonstrate that cool coating materials function not only as a local surface-cooling measures but also as modifiers of the three-dimensional radiative exchange, exerting strong control over the outdoor thermal environment. Depending on how the radiative properties of vertical (building facades) and horizontal (ground) elements are combined, the urban microclimate responds in contrasting ways. Ground-only modifications (raising reflectance) lowered pedestrian-height air temperature during both day and night, supporting the mitigation of both heatwaves and tropical nights. Facade-only and combined modifications introduced nighttime warming in certain pockets via stronger longwave coupling, yet produced more extensive daytime cooling. However, lower air temperature does not necessarily translate into improved thermal comfort; under high-reflectance treatments, amplified multiple reflections can raise radiant load and offset convective cooling [28,35,111,112]. Outdoor design should therefore account for the asymmetry between daytime and nighttime air temperature responses as well as the overall radiative environment. Because thermal comfort depends on radiation, wind speed, and humidity in addition to air temperature, we employ the Universal Thermal Climate Index (UTCI) for an integrated assessment.

3.3. *Outdoor thermal comfort at pedestrian height*

In the central walkway of Gwanghwamun Square (open space), the daytime (08:00–18:00 LST) and nighttime (24:00–07:00 LST) UTCI in CNTL were 26.07℃ and 14.86℃, respectively, generally falling within the ‘no thermal stress’ category (Fig. 16). Between 12:00 LST and 17:00 LST, direct solar exposure elevated T_{mrt} and pushed UTCI into the ‘moderate heat stress’ category. In BcGj, nighttime UTCI decreased slightly by 0.02℃–0.65℃, consistent with the weak nighttime air temperature reductions resulting from reduced daytime heat storage (due to higher reflectance) and/or enhanced nocturnal longwave emission. By contrast, daytime UTCI increased (up to + 2.22℃ in BcG3) due to T_{mrt}

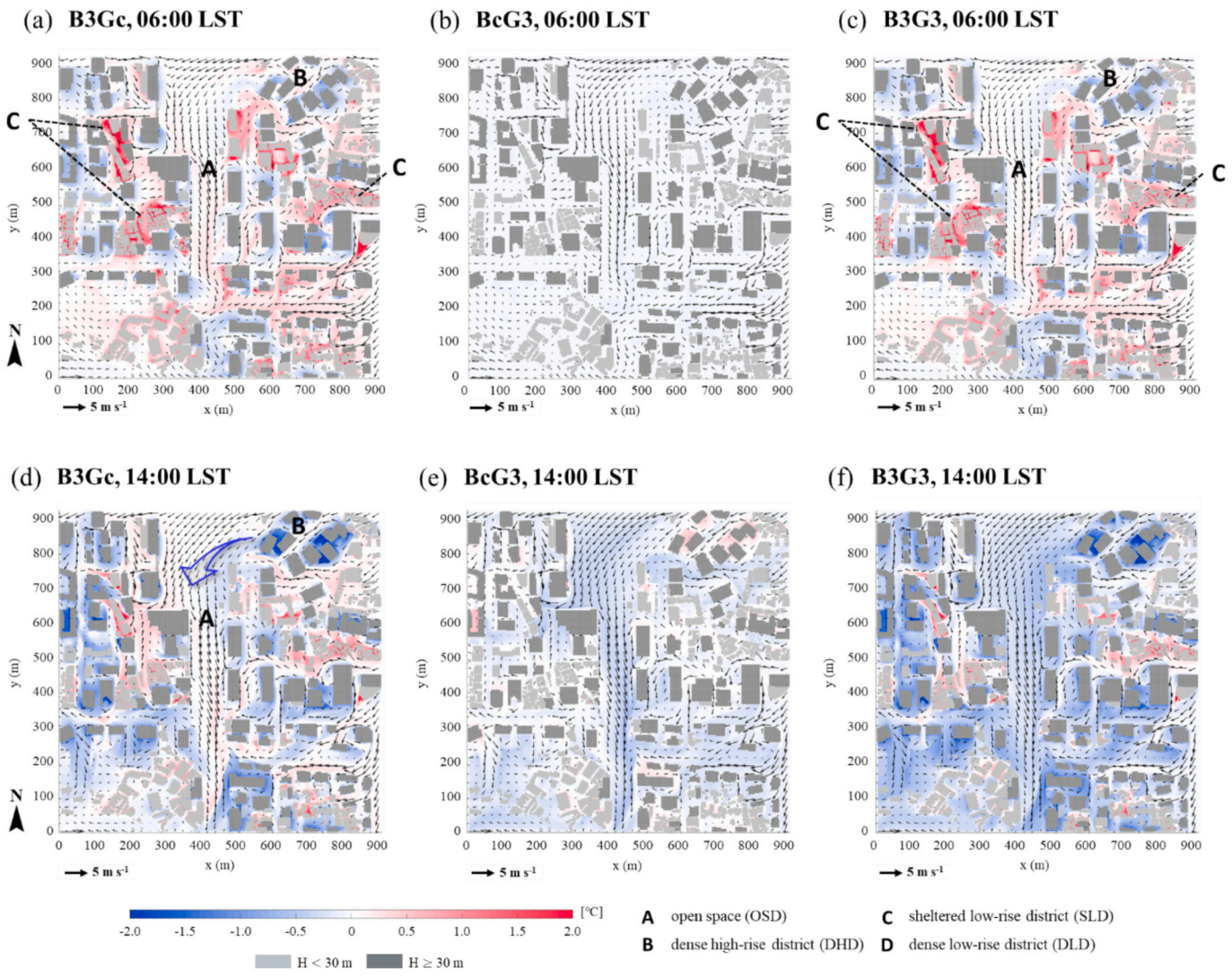

Fig. 15. Wind vectors and contours of air temperature differences relative to control experiment (CNTL) at pedestrian height (1.5 m) in [(a), (d)] B3Gc, [(b), (e)] BcG3, and [(c), (f)] B3G3 at 06:00 LST (upper panels) and 14:00 LST (local standard time) (lower panels) on September 7, 2015. Light grey indicates buildings lower than 30 m, while dark grey represents buildings higher than 30 m. Annotations A, B, C, and D indicate the open space (OSD), dense high-rise (DHD), sheltered low-rise (SLD), and dense low-rise districts (DLD), respectively.

elevations from intensified shortwave reflections, occasionally reaching 'strong heat stress' category during 13:00–15:00 LST, though remaining 'moderate heat stress' category for most daytime hours. In BiGc, the average UTCI increased by 2.8℃ (day) and 4.13℃ (night), with 'strong heat stress' frequently occurring between 13:00 LST and 16:00 LST and an approximately one-hour extension of stress duration in both day and night. In BiGj, UTCI increased by 3.9℃ (day) and 3.7℃ (night), with 'strong heat stress' persisting from ~ 12:00 LST to 16:00 LST. Across all experiments, these patterns indicate that radiant energy emitted or reflected from high-reflectance facades and ground surfaces can elevate T_{mrt} sufficiently to outweigh the modest convective cooling provided by lower air temperature, thereby degrading overall pedestrian thermal comfort. Crucially, this comfort penalty was significantly more pronounced in facade-focused scenarios, whereas ground-only strategies exhibited a relatively moderate trade-off. The relative advantage of ground-only strategies over facade treatments is particularly evident in this open space, where pedestrians are directly exposed to the high-intensity secondary reflections from vertical surfaces. While absolute UTCI values may vary slightly on a local scale depending on pedestrian location, orientation, and density, these factors did not influence the overall UTCI variability—specifically, the relative changes across scenarios—resulting from the application of cool coatings (not shown).

Overall, during summer, high-reflectance cool coatings effectively lowered surface temperatures and, in some locations, air temperatures at pedestrian height. However, increased shortwave reflections can enter pedestrians' field of view or elevate T_{mrt} and UTCI [34,113]. Therefore, cool-coating strategies should balance the direct surface-cooling benefits against the accompanying radiative penalties and local usage patterns. In high density pedestrian corridors, design measures that reduce exposure to reflected radiation (e.g., shading devices, vegetative canopies, low-gloss finishes) are recommended, whereas in low-activity areas, the larger surface-cooling gains may be prioritized. These findings underscore the need for spatially adaptive deployment of cool coatings, tailored to site-specific radiative environments, pedestrian activity, and desired comfort outcomes. While previous studies have often simplified urban radiative environments—by assuming uniform albedo or examining isolated building geometries—this study advances the field by simultaneously modifying the radiative properties of both building facades and ground surface, and by analyzing the resulting thermal fields and pedestrian-height comfort within a high-density urban district.

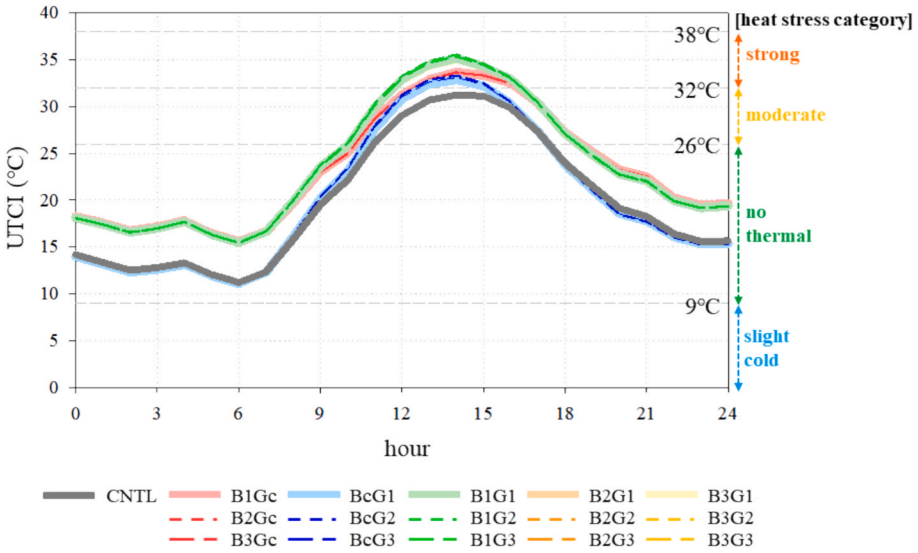

Fig. 16. Time series of Universal Thermal Climate Index (UTCI) at the central pedestrian walkway of Gwanghwamun Square in control experiment (CNTL) and the sensitivity experiments.

3.4. Integrated sensitivity analysis of radiative properties

In high-density urban areas characterized by diverse building heights, such as the target area, we conducted an integrated analysis of how variations in radiative properties (reflectance and emissivity) resulting from cool coating applications influence surface temperatures and pedestrian thermal comfort. In particular, heatmaps were analysed to identify the non-linear interactions between variables, specifically considering the significant increase in emissivity (from 0.03 to 0.90) that occurs when cool coatings are applied to high-rise facades. Fig. 17 presents the distribution of daily mean surface temperatures (facade, roof, and ground) and daily mean UTCI according to various combinations of facade and ground reflectance.

Regarding surface temperatures, the ground-only cool-coating scenarios (BcGj) showed that building surface temperatures either increased slightly or remained similar to CNTL (Fig. 17a and 17b). In contrast, facade-involved scenarios (BiGc, BiGj) yielded opposing results: while high-rise facade temperatures significantly decreased due to enhanced surface cooling from increased reflectance and emissivity, the temperatures of adjacent low-rise buildings increased. This phenomenon occurs because the reflected shortwave and emitted longwave radiation from the high-rise facades are transferred to nearby low-rise surfaces. This radiative energy redistribution also led to an increase in low-rise roof temperatures (Fig. 17c). For the ground surface, while BcGj successfully reduced temperatures, the facade-only scenario (BiGc) resulted in higher ground temperatures than CNTL, as reflected shortwave radiation from high-reflectance facades was intercepted by the ground.

Pedestrian outdoor thermal comfort exhibited trends distinct from surface temperature variations. All cool coating scenarios showed an increase in the daily mean UTCI compared to CNTL (Fig. 17f). In the ground-only cool-coating scenarios (BcGj), despite the reduction in ground surface temperature, the UTCI increased slightly because reflected shortwave radiation reached pedestrians; however, this increase remained limited. Conversely, facade-involved scenarios (BiGc, BiGj) led to a more pronounced increase in UTCI. This is attributed to the intensified T_{mrt} at the pedestrian height, caused by both the increased shortwave reflection and the substantial rise in longwave emission from the high-rise buildings surrounding Gwanghwamun Square. Notably, the highest UTCI was observed in the combined facade-and-ground scenario (BiGj).

Consequently, while cool coatings are effective for cooling targeted surfaces, their application in high-density urban canyons can be disadvantageous for pedestrian thermal comfort due to the redistribution of radiative energy. These results confirm a clear trade-off between surface cooling and outdoor thermal comfort. Facade cool coatings pose a risk of exacerbating heat stress through intense radiative reflection and emission toward the street, whereas ground cool coatings can effectively lower surface temperatures with a relatively minimal adverse impact on thermal comfort. Therefore, for high-density urban canyons similar to the target area, establishing a ground-centric cool coating strategy is identified as the most rational approach for promoting a sustainable urban thermal environment.

4. Conclusions

This study evaluated how modifying the radiative properties of building facades and ground surfaces shapes the urban thermal environment in densely built districts of Jongno-gu and Jung-gu, Seoul, using coupled CitySim Pro–CFD simulations. The CitySim Pro model resolved spatiotemporal surface temperatures from detailed geometry and shortwave and longwave exchanges. These temperatures were then prescribed as boundary conditions in the CFD model to simulate wind and air temperature at pedestrian height, enabling a joint assessment of microclimate and outdoor thermal comfort.

The control experiment (CNTL), representing existing materials, was validated against in-situ surface-temperature and meteorological observations. Sensitivity experiments increased reflectance, and where applicable longwave emissivity, by applying ceramic-based coatings to high-rise facades and cool paints to low-rise facades and ground. In CNTL, surface-temperature patterns reflected material optics, solar position, and shading. During daytime, higher reflectance reduced shortwave absorption and generally cooled treated surfaces, while multiple reflections and shading produced strong spatial heterogeneity. During nighttime, higher emissivity enhanced radiative cooling, whereas low-emissivity high-rise facades retained stored heat and remained warmer than the high-emissivity low-rise facades and ground surfaces. Across experiments, raising reflectance generally cooled the targeted surface but could warm adjacent surfaces through intensified shortwave reflections (radiative feedback). Ground-only modifications produced domain-mean air temperature reductions by day and by night, although the magnitude was small, suggesting mitigation of heatwaves and tropical nights. Facade-only or combined facade–ground modifications sometimes yielded localized nighttime warming through enhanced

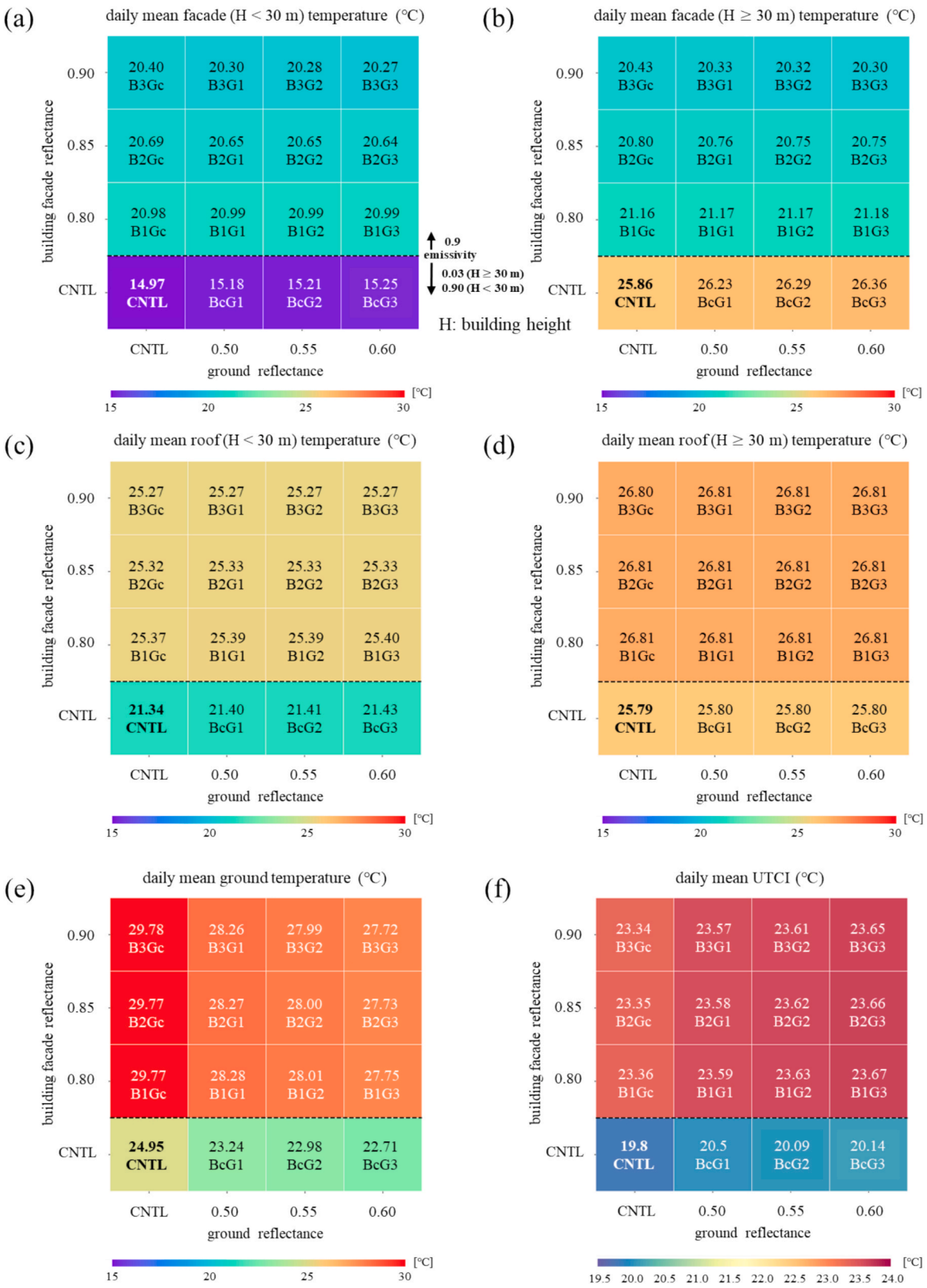

Fig. 17. Heatmaps of daily mean facade temperatures [(a) and (b)], roof temperatures [(c) and (d)], (e) ground temperature, and (f) Universal Thermal Climate Index (UTCI) in control experiment (CNTL) and sensitivity experiments. The black dashed lines indicate the emissivity settings for high-rise and low-rise buildings, and H denotes building height.

longwave coupling, yet delivered broader daytime cooling up to about 2.0 ℃. Overall, the efficacy of cool coatings was spatiotemporally variable due to re-reflection and radiation trapping.

Outdoor thermal comfort was evaluated with the Universal Thermal Climate Index (UTCI), which integrates convective and radiative components, along the central transect of Gwanghwamun Square. In CNTL, UTCI generally fell within no to moderate heat stress, with midday solar exposure elevating stress. Ground-only treatments largely maintained CNTL-like UTCI, aside from some daytime increases associated with higher mean radiant temperature. In contrast, facade-only and combined cases more consistently increased daytime UTCI due to intensified radiative exposure, indicating that lower air temperature does not necessarily translate into improved thermal comfort when radiant load rises.

Ground-focused cool coatings can lower air temperature with minimal comfort penalties, whereas facade coatings require stringent control of reflected radiation. Effective mitigation strategies must balance surface-cooling benefits against radiative penalties and be tailored to specific site functions. In high-traffic corridors, cool coatings should be integrated with measures that minimize exposure to reflected radiation, such as shading devices, vegetative canopies, or low-gloss and low-specular finishes. In low-activity areas, however, larger surface-cooling gains may be prioritized for broader microclimatic and energy benefits. Because horizontal and vertical elements interact radiatively, the combination of ground and facade treatments must be planned with careful consideration of local geometry and pedestrian activity. As supported by previous literature and corroborated by our results, the thermal comfort benefits of ground-cool coatings are maximized in open spaces, consistent with established findings in the literature. Conversely, in deep canyons, a more nuanced application tailored to local geometric characteristics is required to mitigate potential radiative penalties and ensure overall pedestrian well-being.

This study has several limitations that provide a basis for future work. Specifically, urban vegetation was not explicitly represented in this study, which likely leads to an underestimation of the synergistic effects of shading, evapotranspiration, and the resulting reductions in mean radiant temperature. Given that the interactions between cool surfaces and greenery can further modulate the urban microclimate, future work should incorporate species-specific, three-dimensional canopy models. These models should account for dynamic physiological processes, such as stomatal conductance and seasonal phenology, to achieve a more integrated assessment of urban heat mitigation strategies. The simulations focused on a single summer episode, so broader generalizability and robustness require multi-season and multi-year experiments across contrasting climate regimes. Specifically, under extreme heatwave conditions, the trade-off between the surface cooling effect of cool coatings and the deterioration of the radiative environment can be further intensified due to reduced convective heat dissipation. Furthermore, the impact of cool coatings may vary under different wind regimes, as fluctuations in convective heat transfer coefficients and ventilation efficiency within urban canyons modify the surface energy balance. Only outdoor conditions were evaluated; coupled assessments linking outdoor microclimate mitigation to indoor thermal performance and building energy use are necessary. Specifically, detailed HVAC system efficiencies of individual buildings should be considered to accurately predict actual energy consumption and the associated CO_2 emission reduction potential of cool coatings. Additionally, since material properties were treated as static, follow-on studies should account for the effects of aging and soiling, characterize angular and spectral reflectance and emissivity, and improve mean radiant temperature estimation through further field validation and uncertainty analysis.

Overall, enhancing ground-surface reflectance offers a robust, low-penalty pathway to reduce surface and air temperatures, whereas facade treatments can deliver larger daytime cooling but may raise radiant exposure, especially in busy pedestrian spaces. Spatially adaptive deployment, ground-focused with supplemental shading in high-use areas and broader use in low-use areas, provides a practical route to reconcile microclimate cooling with pedestrian thermal comfort.

CRediT authorship contribution statement

Da−Som Mun: Writing – original draft, Visualization, Validation, Methodology, Investigation, Formal analysis, Data curation, Conceptualization. **Jérôme Henri Kämpf:** . **Jae−Jin Kim:** Writing – review & editing, Supervision, Software, Funding acquisition, Formal analysis, Conceptualization.

Declaration of competing interest

We wish to confirm that there are no known conflicts of interest associated with this publication and there has been no significant financial support for this work that could have influenced its outcome.

We confirm that the manuscript has been read and approved by all named authors and that there are no other persons who satisfied the criteria for authorship but are not listed. We further confirm that the order of authors listed in the manuscript has been approved by all of us. We confirm that we have given due consideration to the protection of intellectual property associated with this work and that there are no impediments to publication, including the timing of publication, with respect to intellectual property. In so doing we confirm that we have followed the regulations of our institutions concerning intellectual property.

We understand that the Corresponding Author is the sole contact for the Editorial process (including Editorial Manager and direct communications with the office). He is responsible for communicating with the other authors about progress, submissions of revisions and final approval of proofs. We confirm that we have provided a current, correct email address which is accessible by the Corresponding Author and which has been configured to accept email from jjkim@pknu.ac.kr.

Acknowledgements

This work was supported by the Korea Meteorological Administration Research and Development Program under grant RS-2017-KMI172410 and by the National Research Foundation of Korea (NRF) grant funded by the Korea government (MSIT) (RS-2024-00341302).

Appendix A. Supplementary data

Supplementary data to this article can be found online at https://doi.org/10.1016/j.enbuild.2026.117245.

Data availability

No data was used for the research described in the article.

References

[1] C.D. Ziter, E.J. Pedersen, C.J. Kucharik, M.G. Turner, Scale-dependent interactions between tree canopy cover and impervious surfaces reduce daytime urban heat during summer, Proc. Natl. Acad. Sci. 116 (15) (2019) 7575–7580.
[2] L.R. Rodríguez, J.S. Ramos, F.J.S. de la Flor, S.Á. Domínguez, Analyzing the urban heat Island: Comprehensive methodology for data gathering and optimal design of mobile transects, Sustain. Cities Soc. 55 (2020) 102027.
[3] J. Kong, Y. Zhao, D. Strebel, K. Gao, J. Carmeliet, C. Lei, Understanding the impact of heatwave on urban heat in greater Sydney: temporal surface energy budget change with land types, Sci. Total Environ. 903 (2023) 166374.
[4] X. Bai, Z. Yu, B. Wang, Y. Zhang, S. Zhou, X. Sha, S. Li, X. Yao, X. Geng, 'Quantifying threshold and scale response of urban air and surface temperature to surrounding landscapes under extreme heat, Build. Environ. 247 (2024) 111029.
[5] M. Morabito, A. Crisci, G. Guerri, A. Messeri, L. Congedo, M. Munafò, Surface urban heat islands in italian metropolitan cities: tree cover and impervious surface influences, Sci. Total Environ. 751 (2021) 142334.
[6] A. Ossola, G.D. Jenerette, A. McGrath, W. Chow, L. Hughes, M.R. Leishman, Small vegetated patches greatly reduce urban surface temperature during a summer

heatwave in Adelaide, Australia. Landscape and Urban Planning 209 (2021) 104046.
[7] N.S.M. Harmay, M. Choi, Effects of heat waves on urban warming across different urban morphologies and climate zones, Build. Environ. 209 (2022) 10867.
[8] Z. Shi, X. Li, T. Hu, B. Yuan, P. Yin, D. Jiang, Modeling the intensity of surface urban heat island based on the impervious surface area, Urban Clim. 49 (2023) 101529.
[9] Y. Wei, H. Chen, J.J. Huang, Response of surface energy components to urban heatwaves and its impact on human comfort in coastal city, Urban Clim. 54 (2024) 101836.
[10] T.P. Scolaro, E. Ghisi, Assessing the Energy and Economic Performance of Green and cool Roofs: a Life Cycle Approach, Sustainability 17 (13) (2025) 5782.
[11] N. Nazarian, N. Dumas, J. Kleissl, L. Norford, Effectiveness of cool walls on cooling load and urban temperature in a tropical climate, Energ. Buildings 187 (2019) 144–162.
[12] J. Wang, S. Liu, Z. Liu, X. Meng, C. Xu, W. Gao, An experimental comparison on regional thermal environment of the high-density enclosed building groups with retro-reflective and high-reflective coatings, Energ. Buildings 259 (2022) 111864.
[13] M. Chaumont, M. Hendel, F. Filaine, L. Royon, Influence of the thermal insulation position in standard and cool roofs on their contribution to urban heating during heatwaves, Energ. Buildings 324 (2024) 114907.
[14] S. Khorat, D. Das, R. Khatun, S.M. Aziz, P. Anand, A. Khan, M. Santamouris, D. Niyogi, Cool roof strategies for urban thermal resilience to extreme heatwaves in tropical cities, Energ. Buildings 302 (2024) 113751.
[15] M.A. Alim, Z. Tao, H.M. Imran, M.A. Rahim, Z. Malik, A. Rahman, A scoping review on reflective coatings with nanomaterials: progress since 2000 and current challenges, J. Clean. Prod. 511 (2025) 145633.
[16] M. Santamouris, A. Synnefa, T. Karlessi, Using advanced cool materials in the urban built environment to mitigate heat islands and improve thermal comfort conditions, Sol. Energy 85 (12) (2011) 3085–3102.
[17] L. Gobatti, P.M. Bach, M. Maurer, J.P. Leitão, Impact of soil moisture content on urban tree evaporative cooling and human thermal comfort, Npj Urban Sustainability 5 (1) (2025) 26.
[18] Y.Y. Wei, C.Y. Cheng, T.P. Lin, The influence of trees shade level on human thermal comfort and the development of applied assessment tools, Landsc. Urban Plan. 263 (2025) 105436.
[19] A. Synnefa, M. Santamouris, K. Apostolakis, On the development, optical properties and thermal performance of cool colored coatings for the urban environment, Sol. Energy 81 (4) (2007) 488–497.
[20] U. Berardi, M. Garai, T. Morselli, Preparation and assessment of the potential energy savings of thermochromic and cool coatings considering inter-building effects, Sol. Energy 209 (2020) 493–504.
[21] K. Mehaoued, B. Lartigue, Influence of a reflective glass facade on surrounding microclimate and building cooling load: Case of an office building in Algiers, Sustain. Cities Soc. 46 (2019) 101443.
[22] A. Aboelata, Reducing outdoor air temperature, improving thermal comfort, and saving buildings' cooling energy demand in arid cities–cool paving utilization, Sustain. Cities Soc. 68 (2021) 102762.
[23] E.K.K. Donthu, Y.P. Long, M.P. Wan, M. Zhou, B.F. Ng, Dynamics of cool surface performance on urban microclimate: a full-scale experimental study in Singapore, Sustain. Cities Soc. 102 (2024) 105218.
[24] Q. Li, X. Zhang, J. Hang, Numerical investigations of cool coatings on building envelopes for urban heat mitigation with various street aspect ratios, Sustain. Cities Soc. 107 (2024) 105410.
[25] J. Hang, M. Lu, L. Ren, H. Dong, Y. Zhao, N. Zhao, Cooling performance of near-infrared and traditional high-reflective coatings under various coating modes and building area densities in 3D urban models: scaled outdoor experiments, Sustain. Cities Soc. 106200 (2025).
[26] X. Su, Y. Luo, L. Zhang, The synthetical effects of passive radiative cooling building envelopes and surrounding buildings on building daylighting and energy performance: a case study in Miami, Sustain. Cities Soc. 106190 (2025).
[27] H. Shen, H. Tan, A. Tzempelikos, The effect of reflective coatings on building surface temperatures, indoor environment and energy consumption—An experimental study, Energ. Buildings 43 (2–3) (2011) 573–580.
[28] P.J.C. Schrijvers, H.J.J. Jonker, S.R. De Roode, S. Kenjereš, The effect of using a high-albedo material on the Universal Temperature climate Index within a street canyon, Urban Clim. 17 (2016) 284–303.
[29] O. Mansouri, R. Belarbi, F. Bourbia, Albedo effect of external surfaces on the energy loads and thermal comfort in buildings, Energy Procedia 139 (2017) 571–577.
[30] N. Nazarian, J. Kleissl, CFD simulation of an idealized urban environment: thermal effects of geometrical characteristics and surface materials, Urban Clim. 12 (2015) 141–159.
[31] N. Nazarian, T. Sin, L. Norford, Numerical modeling of outdoor thermal comfort in 3D, Urban Clim. 26 (2018) 212–230.
[32] P.Y. Lai, J.H. Koh, W.S. Koh, H. Liu, Effectively modeling surface temperature and evaluating mean radiant temperature in tropical outdoor industrial environments, Build. Environ. 169 (2020) 106277.
[33] J. Yuan, S. Masuko, Y. Shimazaki, T. Yamanaka, T. Kobayashi, Evaluation of outdoor thermal comfort under different building external-wall-surface with different reflective directional properties using CFD analysis and model experiment, Build. Environ. 207 (2022) 108478.
[34] V.P. Lopez-Cabeza, S. Alzate-Gaviria, E. Diz-Mellado, C. Rivera-Gomez, C. Galan-Marin, Albedo influence on the microclimate and thermal comfort of courtyards under Mediterranean hot summer climate conditions, Sustain. Cities Soc. 81 (2022) 103872.
[35] O. Ahmadizadeh, R. Vakilinezhad, Evaluating the effect of urban surfaces albedo on the microclimate and outdoor thermal comfort in hot climate, Int. J. Environ. Stud. (2024) 1–25.
[36] J. Yuan, D. Yan, X. Xiao, Y. Shimazaki, Y. Wang, Z. Jiao, Z. Lin, M. Bizjak, C. Farnham, K. Emura, Mitigating urban heat islands: Enhancing outdoor comfort with retro-reflective building materials through computational-fluid-dynamics analysis, Next Research 100 (2025) 100199.
[37] Z. Jandaghian, U. Berardi, Analysis of the cooling effects of higher albedo surfaces during heat waves coupling the Weather Research and forecasting model with building energy models, Energ. Buildings 207 (2020) 109627.
[38] Z. Gholami, S. Jalilisadrabad, R. Amrollahi, Investigating the impact of using modified cool materials by titanium dioxide (TiO2)-based photocatalytic self-cleaning nanoparticles in urban facades on urban microclimate parameters, Case Stud. Constr. Mater. 19 (2023) e02268.
[39] H. Elmagri, T.M. Kamel, H. Ozer, Assessment of the effectiveness of cool pavements on outdoor thermal environment in urban areas, Build. Environ. 266 (2024) 112095.
[40] World Meteorological Organization. (2023). WMO report documents spiralling weather and climate impacts. Retrieved from https://wmo.int/news/media-centre/wmo-report-documents-spiralling-weather-and-climate-impacts. Accessed March 19, 2025.
[41] G. Evola, V. Costanzo, C. Magrì, G. Margani, L. Marletta, E. Naboni, A novel comprehensive workflow for modelling outdoor thermal comfort and energy demand in urban canyons: results and critical issues, Energ. Buildings 216 (2020) 109946.
[42] Zhu, Y., & Salvalai, G. (2025, August). Urban building energy simulation for performance analysis of an energy community model in the Italian context. In Building Simulation 2025 (Vol. 19, pp. 0-0). IBPSA.
[43] N. Alchapar, J. Balter, M.V. Mercado, E. Correa, Microclimatic models and their implications on the energy requirements of buildings in warm dry urban areas, Energ. Buildings 319 (2024) 114468.
[44] D. Nascimento, A. Ascenso, D. Lopes, M. Lopes, V. Rodrigues, CFD modelling of an urban microclimate during a heat wave: Coupling solar radiation and heat transfer, Urban Clim. 62 (2025) 102486.
[45] Robinson, D., Haldi, F., Leroux, P., Perez, D., Rasheed, A., & Wilke, U. (2009). CitySim: Comprehensive micro-simulation of resource flows for sustainable urban planning. In Proceedings of the Eleventh International IBPSA Conference (pp. 1083-1090).
[46] N. Yaghoobian, J. Kleissl, An indoor–outdoor building energy simulator to study urban modification effects on building energy use–Model description and validation, Energ. Buildings 54 (2012) 407–417.
[47] R. Zhang, K.P. Lam, S.C. Yao, Y. Zhang, Coupled EnergyPlus and computational fluid dynamics simulation for natural ventilation, Build. Environ. 68 (2013) 100–113.
[48] X. Shan, N. Luo, K. Sun, T. Hong, Y.K. Lee, W.Z. Lu, Coupling CFD and building energy modelling to optimize the operation of a large open office space for occupant comfort, Sustain. Cities Soc. 60 (2020) 102257.
[49] W. Guo, S. Liang, Y. He, W. Li, B. Xiong, H. Wen, Combining EnergyPlus and CFD to predict and optimize the passive ventilation mode of medium-sized gymnasium in subtropical regions, Build. Environ. 207 (2022) 108420.
[50] Y. Fan, K. Ito, Energy consumption analysis intended for real office space with energy recovery ventilator by integrating BES and CFD approaches, Build. Environ. 52 (2012) 57–67.
[51] R. Aghamolaei, M. Fallahpour, P.A. Mirzaei, Tempo-spatial thermal comfort analysis of urban heat island with coupling of CFD and building energy simulation, Energ. Buildings 251 (2021) 111317.
[52] M. Fallahpour, R. Aghamolaei, R. Zhang, P.A. Mirzaei, Outdoor thermal comfort in urban neighbourhoods by coupling of building energy simulation and computational fluid dynamics, Build. Environ. 225 (2022) 109599.
[53] J. Allegrini, V. Dorer, J. Carmeliet, Coupled CFD, radiation and building energy model for studying heat fluxes in an urban environment with generic building configurations, Sustain. Cities Soc. 19 (2015) 385–394.
[54] J. Allegrini, J. Carmeliet, Simulations of local heat islands in Zürich with coupled CFD and building energy models, Urban Clim. 24 (2018) 340–359.
[55] G. Chen, L. Rong, G. Zhang, Comparison of urban airflow between solar-induced thermal wall and uniform wall temperature boundary conditions by coupling CitySim and CFD, Build. Environ. 172 (2020) 106732.
[56] G. Chen, L. Rong, G. Zhang, Unsteady-state CFD simulations on the impacts of urban geometry on outdoor thermal comfort within idealized building arrays, Sustain. Cities Soc. 74 (2021) 103187.
[57] N. Liu, L. Morawska, Modeling the urban heat island mitigation effect of cool coatings in realistic urban morphology, J. Clean. Prod. 264 (2020) 121560.
[58] J. Yang, Z.H. Wang, K.E. Kaloush, Environmental impacts of reflective materials: is high albedo a 'silver bullet'for mitigating urban heat island? Renew. Sustain. Energy Rev. 47 (2015) 830–843.
[59] Kämpf, J. H. (2009). On the modelling and optimisation of urban energy fluxes (Doctoral dissertation, EPFL). https://doi.org/10.5075/epfl-thesis-4362.
[60] G. Mutani, S. Coccolo, J. Kaempf, M. Bilardo, CitySim Guide: Urban Energy Modelling. SUPSI. (2018).
[61] Walter, E., & Kämpf, J. H. (2015, February). A verification of CitySim results using the BESTEST and monitored consumption values. In Proceedings of the 2nd Building Simulation Applications conference (Vol. 2015). Bozen-Bolzano University Press.
[62] J. Allegrini, J. Carmeliet, Coupled CFD and building energy simulations for studying the impacts of building height topology and buoyancy on local urban microclimates, Urban Clim. 21 (2017) 278–305.

[63] D.S. Mun, G. Kang, M. Yang, J.J. Kim, How trees' drag and cooling effects influence airflow and temperature distributions around a street canyon, Build. Environ. 264 (2024) 111913.

[64] D. Mauree, S. Coccolo, J. Kaempf, J.L. Scartezzini, Multi-scale modelling to evaluate building energy consumption at the neighbourhood scale, PLoS One 12 (9) (2017) e0183437.

[65] Franke, J., Hellsten, A., Schlünzen, H., & Carissimo, B. (2007). Best practice guideline for the CFD simulation of flows in the urban environment. COST action 732. Quality Assurance and Improvement of Meteorological Models. University of Hamburg, Meteorological Institute, Center of Marine and Atmospheric Sciences.

[66] M. Ozel, Thermal performance and optimum insulation thickness of building walls with different structure materials, Appl. Therm. Eng. 31 (17–18) (2011) 3854–3863.

[67] I. Adilkhanova, M. Santamouris, G.Y. Yun, Coupling urban climate modeling and city-scale building energy simulations with the statistical analysis: climate and energy implications of high albedo materials in Seoul, Energ. Buildings 290 (2023) 113092.

[68] Y. Qin, Urban canyon albedo and its implication on the use of reflective cool pavements, Energ. Buildings 96 (2015) 86–94.

[69] A. Salvati, M. Kolokotroni, A. Kotopouleas, R. Watkins, R. Giridharan, M. Nikolopoulou, Impact of reflective materials on urban canyon albedo, outdoor and indoor microclimates, Build. Environ. 207 (2022) 108459.

[70] I. Lindseth, A. Bardal, R. Spooren, Reflectance measurements of aluminium surfaces using integrating spheres, Opt. Lasers Eng. 32 (5) (1999) 419–435.

[71] The Engineering ToolBox. (2003). Emissivity coefficients of common materials: Data & reference guide. https://www.engineeringtoolbox.com/emissivity-coefficients-d_447.html.

[72] R.T.A. Prado, F.L. Ferreira, Measurement of albedo and analysis of its influence the surface temperature of building roof materials, Energ. Buildings 37 (4) (2005) 295–300.

[73] M. Jin, S. Liang, An improved land surface emissivity parameter for land surface models using global remote sensing observations, J. Clim. 19 (12) (2006) 2867–2881.

[74] R. Levinson, H. Akbari, P. Berdahl, K. Wood, W. Skilton, J. Petersheim, A novel technique for the production of cool colored concrete tile and asphalt shingle roofing products, Sol. Energy Mater. Sol. Cells 94 (6) (2010) 946–954.

[75] A. Synnefa, T. Karlessi, N. Gaitani, M. Santamouris, D.N. Assimakopoulos, C. Papakatsikas, Experimental testing of cool colored thin layer asphalt and estimation of its potential to improve the urban microclimate, Build. Environ. 46 (1) (2011) 38–44.

[76] Abd El-Raof, H. S., Abd El-Hakim, R. T., El-Badawy, S. M., & Afify, H. A. (2019, November). General Procedure for Pavement Maintenance/Rehabilitation Decisions Based on Structural and Functional Indices. In International Congress and Exhibition" Sustainable Civil Infrastructures" (pp. 13-24). Cham: Springer International Publishing.

[77] C.T. Ruhland, J.A. Niere, The effects of surface albedo and initial lignin concentration on photodegradation of two varieties of *Sorghum bicolor* litter, Sci. Rep. 9 (1) (2019) 18748.

[78] Synnefa, A., Dandou, A., Santamouris, M., & Tombrou, M. (2006a, July). Cool colored coatings for passive cooling of cities. In International Workshop on Energy Performance and Environmental Quality of Buildings (pp. 1-6).

[79] A.L. Pisello, State of the art on the development of cool coatings for buildings and cities, Sol. Energy 144 (2017) 660–680.

[80] Maurizio et al., 2020: Carlini, M., Castellucci, S., Ceccarelli, I., Rotondo, M., & Mennuni, A. (2020). Study of a thermal dispersion in buildings and advantages of ceramic coatings for the reduction of energy expenditure. Energy Reports, 6, 116-128.

[81] E.K.K. Donthu, G.E. Kyriakodis, X. Zhang, Y.P. Long, M.P. Wan, E. Bozonnet, Simulation advances with EnviBatE-A case study on urban heat island mitigation in Singapore, Build. Environ. 258 (2024) 111580.

[82] E.K.K. Donthu, S. Shashwat, K.T. Zingre, M.P. Wan, Development of a simplified cool coating thermal model for predicting street canyon air temperature, Build. Environ. 251 (2024) 111207.

[83] N.H. Gapski, D.L. Marinoski, A.P. Melo, S. Guths, Impact of urban surfaces' solar reflectance on air temperature and radiation flux, Sustain. Cities Soc. 96 (2023) 104645.

[84] A. Synnefa, M. Santamouris, I.J.S.E. Livada, A study of the thermal performance of reflective coatings for the urban environment, Sol. Energy 80 (8) (2006) 968–981.

[85] C. Zhuang, Y. Gao, Y. Zhao, R. Levinson, P. Heiselberg, Z. Wang, R. Guo, Potential benefits and optimization of cool-coated office buildings: a case study in Chongqing, China. Energy 226 (2021) 120373.

[86] M. Carlini, S. Castellucci, I. Ceccarelli, M. Rotondo, A. Mennuni, Study of a thermal dispersion in buildings and advantages of ceramic coatings for the reduction of energy expenditure, Energy Rep. 6 (2020) 116–128.

[87] M. Rawat, R.N. Singh, Performance evaluation of a cool roof model in composite climate, Mater. Today Proc. 44 (2021) 4956–4960.

[88] T. Kinouchi, T. Yoshinaka, N. Fukae, M. Kanda, 4.7 Development of cool pavement with dark colored high albedo coating, Target 50 (40) (2003) 40.

[89] S.R. Griffiths, J.A. Rowland, N.J. Briscoe, P.E. Lentini, K.A. Handasyde, L. F. Lumsden, K.A. Robert, Surface reflectance drives nest box temperature profiles and thermal suitability for target wildlife, PLoS One 12 (5) (2017) e0176951.

[90] M. Sleiman, G. Ban-Weiss, H.E. Gilbert, D. François, P. Berdahl, T.W. Kirchstetter, H. Destaillats, R. Levinson, Soiling of building envelope surfaces and its effect on solar reflectance—Part I: Analysis of roofing product databases, Sol. Energy Mater. Sol. Cells 95 (12) (2011) 3385–3399.

[91] H. Takebayashi, K. Miki, K. Sakai, Y. Murata, T. Matsumoto, S. Wada, T. Aoyama, Experimental examination of solar reflectance of high-reflectance paint in Japan with natural and accelerated aging, Energ. Buildings 114 (2016) 173–179.

[92] R. Paolini, A. Zani, T. Poli, F. Antretter, M. Zinzi, Natural aging of cool walls: Impact on solar reflectance, sensitivity to thermal shocks and building energy needs, Energ. Buildings 153 (2017) 287–296.

[93] D. Shi, C. Zhuang, C. Lin, X. Zhao, D. Chen, Y. Gao, R. Levinson, Effects of natural soiling and weathering on cool roof energy savings for dormitory buildings in chinese cities with hot summers, Sol. Energy Mater. Sol. Cells 200 (2019) 110016.

[94] R. Paolini, G. Terraneo, C. Ferrari, M. Sleiman, A. Muscio, P. Metrangolo, T. Poli, H. Destaillats, M. Zinzi, R. Levinson, Effects of soiling and weathering on the albedo of building envelope materials: Lessons learned from natural exposure in two European cities and tuning of a laboratory simulation practice, Sol. Energy Mater. Sol. Cells 205 (2020) 110264.

[95] K.A. Dornelles, Effect of aging on solar reflectance of white cool roof coatings: natural weathering and the influence on building energy needs for different climate conditions in Brazil, Journal of Architectural Environment & Structural Engineering Research 4 (2) (2021).

[96] European Commission. Photovoltaic Geographical Information System (PVGIS). EU Sci Hub - Eur Comm 2020. https://ec.europa.eu/jrc/en/pvgis (accessed June 20, 2020).

[97] I.P. Castro, D.D. Apsley, Flow and dispersion over topography: a comparison between numerical and laboratory data for two-dimensional flows, Atmos. Environ. 31 (6) (1997) 839–850.

[98] H. Versteeg, W. Malalasekera, An Introduction to Computational Fluid Dynamics: the Finite volume Method, Longman (1995).

[99] Bröde, P., Krüger, E., & Rossi, F. (2011, July). Assessment of urban outdoor thermal comfort by the Universal Thermal Climate Index UTCI. In 14th International Conference on Environmental Ergonomics, Greece.

[100] G.R. McGregor, universal thermal comfort index (UTCI), Int. J. Biometeorol. 56 (3) (2012) 419.

[101] P.K. Cheung, C.Y. Jim, Comparing the cooling effects of a tree and a concrete shelter using PET and UTCI, Build. Environ. 130 (2018) 49–61.

[102] X. Wang, H. Li, S. Sodoudi, The effectiveness of cool and green roofs in mitigating urban heat island and improving human thermal comfort, Build. Environ. 217 (2022) 109082.

[103] T. Xu, R. Yao, C. Du, B. Li, Outdoor thermal perception and heatwave adaptation effects in summer–A case study of a humid subtropical city in China, Urban Clim. 52 (2023) 101724.

[104] S. Zafarmandi, A. Matzarakis, L. Norford, Effects of clothing's thermal insulation on outdoor thermal comfort and thermal sensation: a case study in Tehran, Iran. Sustainable Cities and Society 100 (2024) 104988.

[105] Y. Chen, S. Deng, Y. Hou, Q. Yan, Impact of environmental elements in classical chinese gardens on microclimate and their optimization using ENVI-MET simulations, Energ. Buildings 329 (2025) 115238.

[106] G. Kang, J.J. Kim, How to Plant Trees on an Elevated Road to Improve thermal Comfort in a Street Canyon, Sustain. Cities Soc. 106207 (2025).

[107] D.J. Kim, D.I. Lee, J.J. Kim, M.S. Park, S.H. Lee, Development of a building-scale meteorological prediction system including a realistic surface heating, Atmos. 11 (1) (2020) 67.

[108] M.E. Gavidia-Calderón, S. Ibarra-Espinosa, Y. Kim, Y. Zhang, M.D.F. Andrade, Simulation of O 3 and NO x in Sao Paulo street urban canyons with VEIN (v0. 2.2) and MUNICH (v1. 0), Geosci. Model Dev. Discuss. 2020 (2020) 1–32.

[109] H. Kusaka, H. Kondo, Y. Kikegawa, F. Kimura, A simple single-layer urban canopy model for atmospheric models: Comparison with multi-layer and slab models, Bound.-Lay. Meteorol. 101 (2001) 329–358.

[110] W. Zhu, B. Wu, N. Yan, X. Feng, Q. Xing, A method to estimate diurnal surface soil heat flux from MODIS data for a sparse vegetation and bare soil, J. Hydrol. 511 (2014) 139–150.

[111] S. Falasca, V. Ciancio, F. Salata, I. Golasi, F. Rosso, G. Curci, High albedo materials to counteract heat waves in cities: an assessment of meteorology, buildings energy needs and pedestrian thermal comfort, Build. Environ. 163 (2019) 106242.

[112] C. Chen, J. Wang, H. Zhang, X. Xu, L.E. Hinkle, X. Chao, Q. Shi, Dual impacts of solar-reflective facades in high-density urban areas on building energy use and outdoor thermal environments, Energ. Buildings 324 (2024) 114926.

[113] S.S. Tabatabaei, R. Fayaz, The effect of facade materials and coatings on urban heat island mitigation and outdoor thermal comfort in hot semi-arid climate, Build. Environ. 243 (2023) 110701.